BIOLOGICAL CRYSTALLOGRAPHY

ISSN 1399-0047

In meso in situ serial X-ray crystallography of soluble and membrane proteins

Chia-Ying Huang,[a] Vincent Olieric,[b] Pikyee Ma,[a] Ezequiel Panepucci,[b] Kay Diederichs,[c] Meitian Wang[b]* and Martin Caffrey[a]*

[a]Membrane Structural and Functional Biology Group, Schools of Medicine and Biochemistry and Immunology, Trinity College, Dublin, Ireland, [b]Swiss Light Source, Paul Scherrer Institute, CH-5232 Villigen, Switzerland, and [c]Fachbereich Biologie, Universität Konstanz, M647, D-78457 Konstanz, Germany. *Correspondence e-mail: meitian.wang@psi.ch, martin.caffrey@tcd.ie

Received 30 January 2015
Accepted 13 March 2015

Edited by R. J. Read, University of Cambridge, England

Keywords: AlgE; bromine SAD; experimental phasing; *in meso*; *in situ*; lipid cubic phase; membrane protein; mesophase; $PepT_{St}$; sulfur SAD; serial crystallography.

PDB references: Lyso-Native, 293 K, 4xjb; Lyso-Native, 100 K, 4xjd; Lyso-Br, 293 K, 4xjf; Lyso-Br, 100 K, 4xjg; Lyso-S, 293 K, 4xjh; Lyso-S, 100 K, 4xji; PepTst, 293 K, 4xni; PepTst, 100 K, 4xnj; AlgE, 293 K, 4xnk; AlgE, 100 K, 4xnl

Supporting information: this article has supporting information at journals.iucr.org/d

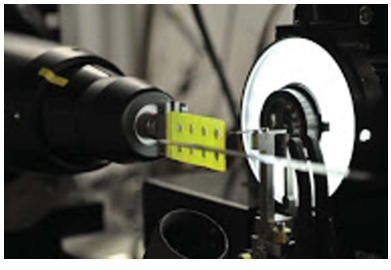

OPEN ACCESS

The lipid cubic phase (LCP) continues to grow in popularity as a medium in which to generate crystals of membrane (and soluble) proteins for high-resolution X-ray crystallographic structure determination. To date, the PDB includes 227 records attributed to the LCP or *in meso* method. Among the listings are some of the highest profile membrane proteins, including the β_2-adrenoreceptor–G_s protein complex that figured in the award of the 2012 Nobel Prize in Chemistry to Lefkowitz and Kobilka. The most successful *in meso* protocol to date uses glass sandwich crystallization plates. Despite their many advantages, glass plates are challenging to harvest crystals from. However, performing *in situ* X-ray diffraction measurements with these plates is not practical. Here, an alternative approach is described that provides many of the advantages of glass plates and is compatible with high-throughput *in situ* measurements. The novel *in meso in situ* serial crystallography (IMISX) method introduced here has been demonstrated with AlgE and PepT (alginate and peptide transporters, respectively) as model integral membrane proteins and with lysozyme as a test soluble protein. Structures were solved by molecular replacement and by experimental phasing using bromine SAD and native sulfur SAD methods to resolutions ranging from 1.8 to 2.8 Å using single-digit microgram quantities of protein. That sulfur SAD phasing worked is testament to the exceptional quality of the IMISX diffraction data. The IMISX method is compatible with readily available, inexpensive materials and equipment, is simple to implement and is compatible with high-throughput *in situ* serial data collection at macromolecular crystallography synchrotron beamlines worldwide. Because of its simplicity and effectiveness, the IMISX approach is likely to supplant existing *in meso* crystallization protocols. It should prove particularly attractive in the area of ligand screening for drug discovery and development.

1. Introduction

Despite its many successes, the lipid cubic phase (LCP) or *in meso* crystallization method still presents significant technical challenges. These derive mainly from the sticky and viscous nature of the cubic mesophase in which the crystals grow and from which they must be harvested for crystallographic data collection. Further, *in meso* crystals are typically small, fragile and radiation-sensitive. Crystallization trials are usually set up in glass sandwich plates either manually or robotically. While glass plates offer many advantages such as optical clarity, non-birefringence and watertight sealing, harvesting from them is not at all trivial. Indeed, it is a cumbersome and tedious process that requires considerable manual dexterity, patience and good fortune. In addition, harvesting is hard to perform reproducibly, is inefficient and can damage the crystals. Harvested crystals are snap-cooled in liquid nitrogen and stored in Dewars for shipping to a synchrotron. As often as

not, the mesophase in which the harvested crystal resides becomes opaque upon snap-cooling. As a result, the crystals are no longer visible when viewed with an on-axis microscope, and diffraction rastering must be used to find and to centre the crystal. Protocols that involve the use of glass-cutting tools have been developed to facilitate harvesting, and instructional online videos are available to assist the novice (Li, Boland, Aragao *et al.*, 2012). Regardless, the method is challenging.

Obviously, then, the prospect of not having to harvest and snap-cool the crystal, but rather being able to collect X-ray diffraction data directly, with the crystal residing unperturbed where it is growing, is hugely attractive. It is the realisation and the implementation of such an *in meso in situ* method that we report here. *In situ* data collection is not new. It has been demonstrated on a number of other crystallization platforms that include vapour-diffusion plates (Bingel-Erlenmeyer *et al.*, 2011; Axford *et al.*, 2012; Cipriani *et al.*, 2012), microfluidic chips (Pinker *et al.*, 2013; Heymann *et al.*, 2014; Perry *et al.*, 2014), acoustically loaded pins (Yin *et al.*, 2014) and microcapillaries (Pineda-Molina *et al.*, 2012), and with nanodroplets (Maeki *et al.*, 2012). However, to date there are but a few examples in which the *in situ* approach has been implemented with *in meso* crystallogenesis. In those instances, convincing evidence that the method yielded a structure or that it could be used for routine, high-throughput data collection was not provided.

The study described here set out to develop a high-throughput *in meso* crystallization platform compatible with *in situ* macromolecular crystallographic (MX) measurements at room temperature with a synchrotron X-ray microbeam. The goal was to perform MX on crystals directly in the mesophase under the conditions in which the crystals grow at 20°C. As a result, cooling to cryogenic (100 K) temperatures, which can degrade diffraction quality, is not required. Another advantage of measurement at ambient temperatures is that the resulting structure models may sample functionally relevant conformations (Woldeyes *et al.*, 2014). However, it does mean that radiation damage is a considerably greater concern since room-temperature data collection is associated with a crystal life dose (Holton, 2009) that is one to two orders of magnitude less than those observed at 100 K. This in turn means that with currently available X-ray flux densities and detectors only a very limited angular range of useful diffraction data can be gathered from a single crystal. This necessitates the collection of many small data wedges from a multitude of randomly oriented crystals in a process that amounts to serial crystallography (SX).

SX is an emerging technique that is well suited to measurements with high-fluence, femtosecond pulses from an X-ray free-electron laser (XFEL) where each crystal is destroyed subsequent to the diffraction event. This method, called serial femtosecond crystallography (SFX; Chapman *et al.*, 2011), has been implemented with LCP-grown crystals, providing structures of challenging G protein-coupled receptors to high resolution (Liu *et al.*, 2013; Weierstall *et al.*, 2014; Fenalti *et al.*, 2015). It has also been used with micro-focused beams at synchrotron sources (Gati *et al.*, 2014; Stellato *et al.*, 2014; Nogly *et al.*, 2015; Botha *et al.*, 2015). SX requires careful selection, sorting and processing of diffraction images to provide suitable data for structure solution and refinement. The data obtained in SX experiments performed to date have had sufficient quality for molecular replacement and structure refinement. However, experimental phasing, which demands the highest quality data, has only been demonstrated in favourable cases where gadolinium, iodine and gold derivatives were used (Barends *et al.*, 2014; Botha *et al.*, 2015).

The objective of the current work was to develop materials and to implement methods that could be used to set up *in meso* crystallization trials robotically in plates that could be used for direct, *in situ* MX data collection at room temperature. Ideally, the plates should enable data collection in support of the more demanding native SAD phasing for structure solution. Because glass that is sufficiently thin to have negligible X-ray absorption and scattering is both hard to handle and expensive, an alternative window material was needed. The synthetic cyclic olefin copolymer (COC) was therefore chosen for several reasons. To begin with, it is commercially available in sheets of varying thicknesses and is inexpensive. Further, it is relatively watertight, optically transparent, UV-transmitting and non-birefringent. As a plastic, COC is chemically inert and is a weak absorber and scatterer of X-rays. Another attractive feature is that it has performed favourably in other *in situ* studies. As described in more detail in §3, the COC sandwich plates developed in the course of this work were designed for use in essentially the same way that standard *in meso* crystallization glass plates are prepared.

While the *in meso* method was designed for use with membrane proteins, it also works with soluble proteins. Accordingly, because of its ease of handling, crystallizability and ready availability, the soluble protein lysozyme was employed for much of the development and proof-of-principle work reported here. The β-barrel alginate transporter AlgE and the α-helical peptide transporter $PepT_{St}$ were used as paradigm integral membrane proteins.

In the following, we describe (i) the COC plates used for *in meso in situ* serial crystallography (IMISX), (ii) how the plates are filled with protein-laden mesophase using an *in meso* robot and then sealed within a glass sandwich plate for incubation and crystal growth, (iii) the mounting of the COC plates on the goniometer and the identification of crystals for analysis within the well using an on-axis microscope, (iv) serial diffraction data collection at room temperature from a chosen set of crystals using a Pilatus 6M-F detector operating at 10–20 Hz, (v) diffraction image selection and data processing, structure solution and refinement, and (vi) a comparison of structures recorded at room and cryogenic temperatures.

We also report structures solved by molecular replacement and experimental phasing. Importantly, we show that the IMISX approach is amenable to native sulfur SAD phasing. It is a highly efficient approach to screen for optimum crystallization conditions and for diffraction data collection that can lead directly to high-resolution structures in ways that require miniscule amounts of protein in a few hundred small crystals

but without the need for harvesting or cryogenic treatment. IMISX also allows data collection from crystals that are too small and/or too fragile to handle.

2. Materials and methods

2.1. Materials

Details of the materials used and their sources are provided in the Supporting Information.

2.2. Methods

2.2.1. Protein-laden mesophase, manual and robot-based crystallization and shipping. Three proteins were used in this study: chicken egg-white lysozyme, the peptide transporter $PepT_{St}$ from *Streptococcus thermophilus* and AlgE, the alginate transporter from *Pseudomonas aeruginosa* (PA01). Lysozyme was obtained from a commercial source and was used as received. $PepT_{St}$ and AlgE were produced recombinantly in *Escherichia coli* and purified from biomass following published protocols (Tan *et al.*, 2014; Lyons *et al.*, 2014). For use in *in meso* crystallization trials, lysozyme-laden mesophase was produced by homogenizing two volumes of lysozyme solution at 50 mg ml^{-1} in Milli-Q water with three volumes of the monoacylglycerol (MAG) lipid monoolein (9.9 MAG) in a coupled-syringe mixing device (Cheng *et al.*, 1998) at 20°C, as described by Caffrey & Cherezov (2009). A similar protocol was used for $PepT_{St}$ and AlgE, with the exception that the hosting lipid used was 7.8 MAG, the lipid:protein solution ratio was 1 and the concentration of the protein solution was 10 mg ml^{-1}. The protein-laden mesophase was dispensed into wells on crystallization plates manually or robotically at 20°C using 50–200 nl mesophase and 800–1000 nl precipitant solution, as described by Caffrey & Cherezov (2009). The robots used included instruments provided by Sias (XANTUS; Cherezov *et al.*, 2004), TTP Labtech (Mosquito LCP) and Art Robbins (Gryphon LCP) (Li, Boland, Walsh *et al.*, 2012). The precipitant solutions used with lysozyme consisted of 0.5–1 *M* NaCl, 50–100 m*M* sodium acetate pH 4.5, 15–30%(*v*/*v*) PEG 400. *In meso*-grown lysozyme crystals dissolve over the course of 2–4 d. They were longer-lived, providing more handling flexibility, when grown at the lower precipitant ingredient concentrations. The $PepT_{St}$ precipitant solutions consisted of 250–325 m*M* $NH_4H_2PO_4$, 100 m*M* HEPES pH 7.0, 21–22%(*v*/*v*) PEG 400. The AlgE precipitant consisted of 350–450 m*M* ammonium chloride, 18–21%(*v*/*v*) PEG 400, 100 m*M* MES buffer pH 5.5–6.5. Additional trials were performed with lysozyme to generate bromide-derivatized crystals. In this case, the NaCl in the precipitant was replaced by 1 *M* NaBr (Dauter & Dauter, 1999).

The method used to produce crystals of lysozyme is based on a 30 min crystallization protocol developed for instructional purposes to demonstrate *in meso* crystallogenesis (Aherne *et al.*, 2012). Because lysozyme is a relatively small water-soluble protein, the crystals that grow are stable for at most a few days in the lipid mesophase. Thereafter, the crystals slowly degrade and disappear, presumably owing to dissolution of the protein in the bathing precipitant solution. Because the crystals are relatively short-lived, most of the lysozyme crystals used in this study were grown on-site at the Swiss Light Source (SLS). In contrast, the $PepT_{St}$ and AlgE crystals, which are stable *in meso* for months, were grown in the Membrane Structural and Functional Biology (MS&FB) laboratory at Trinity College Dublin and were 'express' shipped in double-

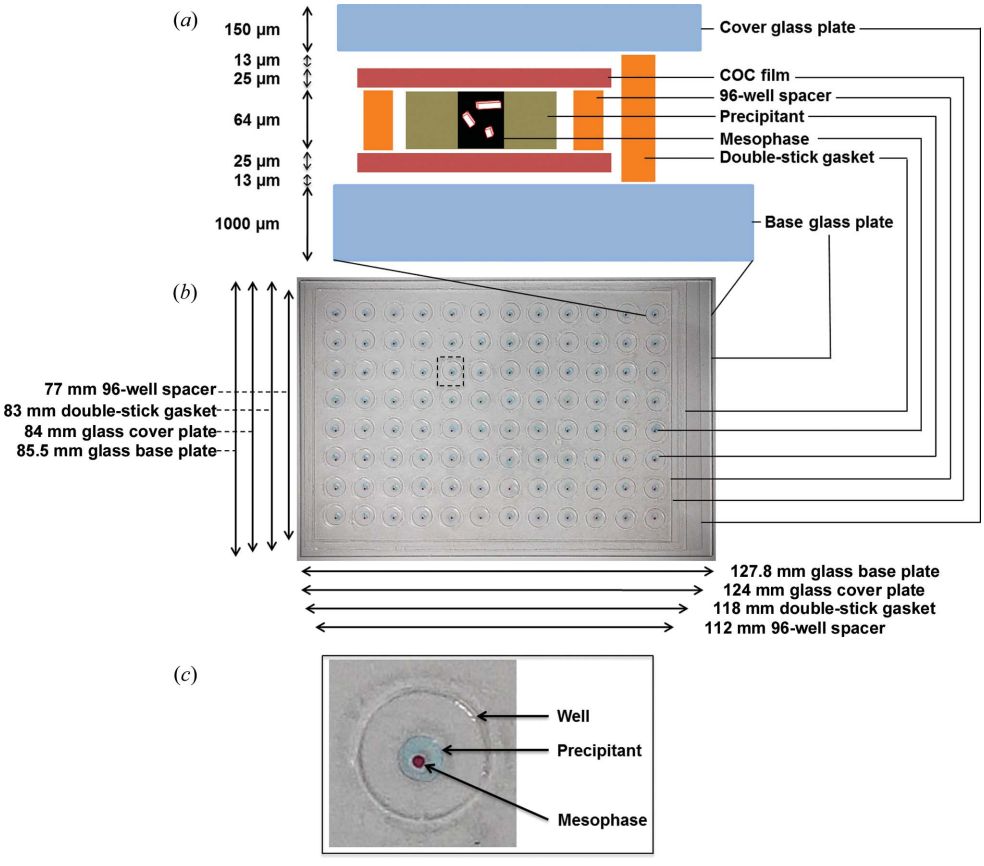

Figure 1
Schematic (*a*) and photographic image (*b*) of a double-sandwich 96-well IMISX plate. The schematic is not drawn to scale. An expanded view of one of the wells is shown in (*c*). To make the mesophase and precipitant more obvious, they were prepared with Sudan Red and blue food dye (Goodalls Blue Colouring containing Brilliant Blue FCF E133 and Carmoisine E122), respectively. The mesophase and precipitant volumes are 100 and 600 nl, respectively. The well diameter is 6 mm.

sandwich plates (see below) to the SLS. Special attention was paid to maintaining the temperature of the plates at 20°C during shipping by surrounding them with large (400 ml) thermal packs pre-equilibrated at 20°C and by crating in thick-walled Styrofoam boxes. Alternatively, similarly packaged plates were taken in checked luggage on direct flights to suitable destinations. Following these procedures, the plates were delivered within 2–3 d intact at 20°C, at which point they were transferred to and stored in a temperature-regulated chamber at 20°C at the SLS until use.

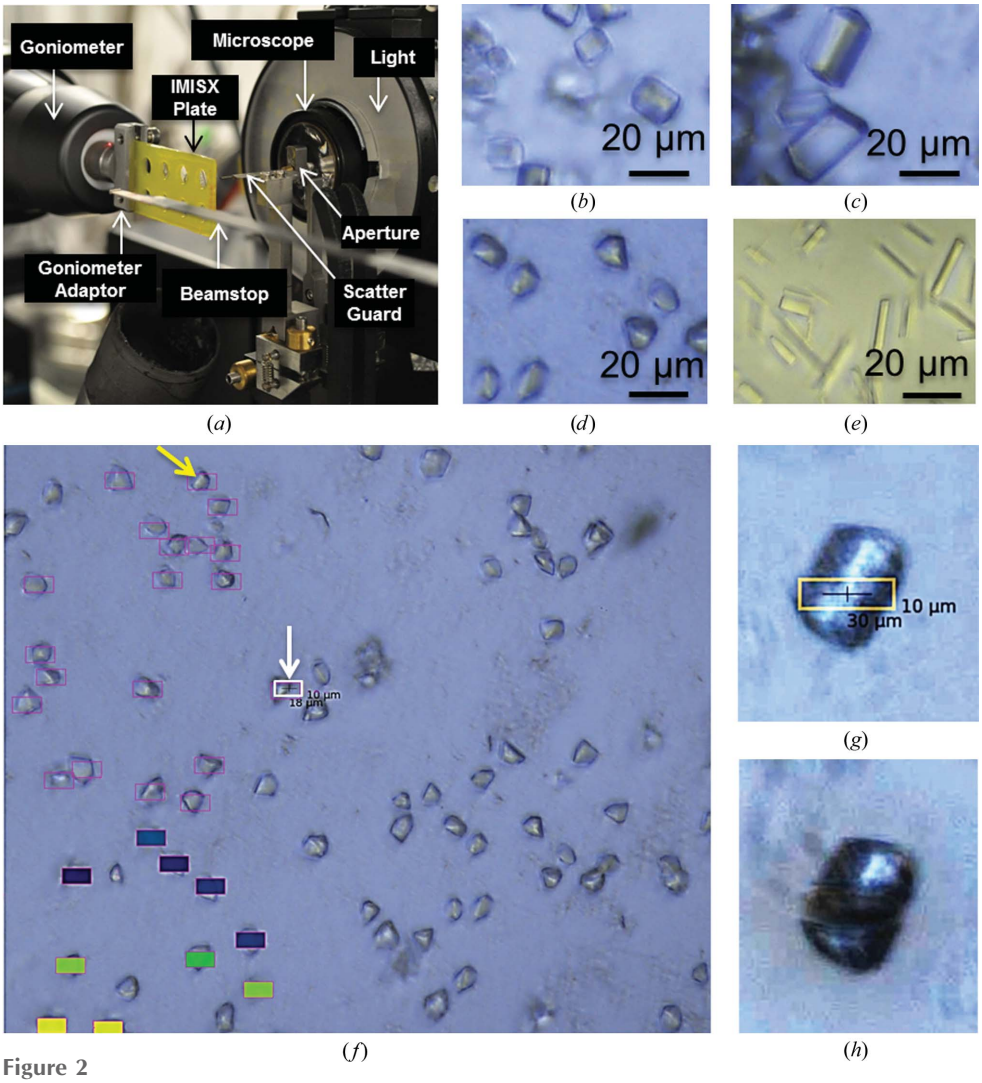

Figure 2
Experimental setup for IMISX data collection and images of crystals grown in IMISX plates. (*a*) A view of a section of an IMISX plate in the goniometer positioned for SX data collection on beamline PXII (X10SA) at the SLS. (*b*–*e*) Crystals of lysozyme (*b*), lysozyme–bromide (*c*), $PepT_{St}$ (*d*) and AlgE (*e*) in COC wells removed from IMISX plates as viewed through the high-resolution on-axis microscope. (*f*) Screenshot of $PepT_{St}$ crystals in a well from an IMISX plate as viewed through the on-axis microscope during SX data collection. Crystals measuring ~10 × 10 µm (yellow arrow) are clearly visible in these *in situ* samples using the high-resolution microscope, which greatly facilitates crystal picking. 'Hand-picking' of crystals is performed at the click of a mouse with the SLS software *DA+* and involves simply positioning a rectangular box (white; white arrow) on the crystal of interest. In this instance, the beam dimensions are 18 × 10 µm. Open boxes correspond to crystals due for data collection. Filled boxes identify crystals that have already been exposed and are colour-coded by the number of reflections detected at that particular site of exposure. (*g*, *h*) Images of a lysozyme crystal before (*g*) and after (*h*) SX data collection. The position of the beam on the crystal and the size of the beam are shown in (*g*). Beam damage to the crystal caused by a 0.5 s exposure at 2.2×10^{12} (12 keV) photons s^{-1} at RT is clearly visible in (*h*). The crystal used in this demonstration of radiation damage is large by comparison with those used for IMISX.

2.2.2. Setting up and using IMISX plates. The COC film used to create the windows of the *in situ* wells is not completely watertight (Supplementary Fig. S1). Accordingly, isolated COC sandwich plates do not provide the same crystal-growing environment as exists in the sealed, standard glass sandwich plates that are used for *in meso* crystallogenesis. In an attempt to replicate, as much as possible, standard crystallization conditions in the new *in situ* plates, it was decided to house the COC plates inside a sealed glass sandwich plate, in what will be referred to as a double-sandwich plate, for the purposes of incubation and crystal growth. The glass plate must subsequently be opened to remove the *in situ* plate, or sections thereof, for SX.

The materials required to prepare a double-sandwich plate include a 124 × 84 mm No. 1.5 glass 0.15 mm thick plate, a 127.8 × 85.5 mm standard 1 mm thick glass plate, two 112 × 77 mm pieces of 25 µm thick COC film with front and back protective covers, a 112 × 77 mm sheet of perforated, 64 or 140 µm thick double-stick spacer tape (6 mm diameter perforations spaced 7 mm apart centre to centre), a double-stick gasket 2 mm wide and 140 µm thick with outer dimensions of 118 × 83 mm and inner dimensions of 114 × 79 mm, Milli-Q water, silanizing agent (RainX), tissue paper, tape, a glass-cutting tool, tweezers, scissors, a scalpel or blade and a brayer or hand-held roller.

The following steps are taken to assemble, fill and seal a double-sandwich plate, to retrieve from it the COC plate containing crystals dispersed in the lipid mesophase and to mount it at the beamline for SX (Fig. 1).

Step 1. Remove the bottom protective cover from the double-stick gasket, place it sticky side down around the edge of the standard 1 mm thick glass plate and brayer it in place to provide a tight seal. This creates the base plate in which the COC plate will be housed and sealed.

Step 2. With the aid of a piece of adhesive tape, remove one of the protective covers from the COC film, treat the exposed

surface with silanizing agent, rinse with water and blot dry with a tissue. This creates the base of the COC sandwich plate.

Step 3. Remove the protective cover from one side of the 112 × 77 mm perforated spacer tape and apply it, sticky side down, to the silanized surface of the COC film from step 2. Use the brayer to produce a tight seal. This step provides the COC base plate plus wells in which crystallization will take place.

Step 4. Place a drop of water on the upper surface of the glass base plate from step 1. This provides a humid atmosphere in the sealed chamber and capillarity with which to hold together parts of the double-sandwich plate. With the aid of a piece of tape, remove the protective cover from the bottom of the COC base plate prepared in step 3 and place it bottom side down firmly onto the glass plate to be held in place by capillarity. Be careful to centre the COC plate within the rectangular gasket seal. Remove the protective cover from the upper surface of the double-stick gasket and the 96-well section of double-stick spacer tape on the glass base plate. This step generates the bottom section of the double sandwich in which the base of the COC plate sits ready for loading with mesophase and precipitant.

Step 5. Remove the protective cover from one side of the second COC film, treat it with silanizing agent and rinse and dry it as in step 2. Remove the second protective cover from the film, place it with its nonsilanized surface down in contact with and centred on the No. 1.5 glass plate to which has been applied a drop of water to bond the two by capillarity. This creates the cover plate with which to seal both the COC plate and the glass sandwich plate.

Step 6. Mount the base plate from step 4 on a desk or on the deck of the *in meso* robot and load protein-laden mesophase and precipitant solution into each of the 96 wells manually or robotically. Seal the filled plate with the cover plate from step 5 with the COC film facing down. Place a standard glass plate on top of the cover plate and brayer to provide tight seals all round. Note that without the standard glass plate, the mesophase bolus can deform by the brayering action and smear the mesophase bolus.

Step 7. Place the double-sandwich plate in a temperature-regulated chamber or an incubator/imager (RockImager RI1500, Formulatrix, Waltham, Massachusetts, USA) at 20°C. Monitor for crystal growth by periodic inspection using bright-field and cross-polarized light microscopy. Record images of the mesophase bolus and the crystals therein to facilitate 'crystal picking' for IMISX at the beamline.

Step 8. With a glass-cutting tool and a straight edge, score lines in the No. 1.5 cover glass of the double-sandwich plate around the COC plate and inside the gasket seal. Remove the freed cover glass and retrieve the delicate COC sandwich plate with tweezers. Apply a section of double-stick spacer tape to one side of the COC sandwich plate to give it structural rigidity for easy handling and stability during SX. Cut the COC plate into sections, typically 1 or 2 × 2 or 3 wells (Fig. 2*a*) for immediate *in situ* SX. Store unused plate sections in a sealed, humid chamber until use. Finally, remove the protective cover from the double-stick tape on the COC section for use in SX and bond it to a suitably sized and perforated piece of rigid 1 mm thick plastic to facilitate mounting.

Step 9. At the beamline, mount the strengthened COC sandwich plate in the magnetic head of the goniometer and orient the plate normal to the beam with the chosen well/bolus positioned in the cross-hairs of the high-resolution on-axis sample-viewing microscope which corresponds to the position of the beam (Fig. 2*a*). (For reference, we define the *X*, *Y* and *Z* positioning of the crystal as follows. *X* corresponds to the crystal position along the rotation axis of the goniometer which is aligned to intersect orthogonally with the X-ray beam axis. *Z* corresponds to the position along the beam axis and *Y* to the position along the axis perpendicular to both *X* and *Z*.) The on-axis microscope has a continuously variable magnification from 2.50-fold to 30-fold. The COC sandwich plate is optically transparent and crystals are clearly visible when viewed *in situ* with the microscope (Figs. 2*b*–2*h*). Adjust the *X*, *Y* and *Z* coordinates of a chosen crystal in the well by means of the motorized goniometer to position the crystal in the focal plane of the microscope that includes the rotation axis of the goniometer and the cross-hairs of the camera/microscope. This ensures that the crystal is in position for data collection, where the axis of rotation of the goniometer, and thus the crystal, is adjusted from 1 to 3°. The SLS data-acquisition software (*DA+*) was used for semi-automated, high-throughput crystal picking (Fig. 2*f*). Crystal positions are recorded for use in subsequent automated, sequential SX data collection. Repeat the crystal-picking process for as many crystals as are required for the collection of a complete data set or are of interest in the chosen well. For large crystals, multiple positions on the same crystal can be selected, taking care to provide a sufficient distance between them to avoid spillover of radiation damage. Data are collected iteratively with due regard to the beam and crystal characteristics. Repeat the 'select/pick and shoot' protocol within a well and extend to additional wells, as needed, until data of sufficient quality and completeness have been collected. The software recognizes which crystals have been X-rayed and avoids reusing them. These are flagged on the computer screen image from the on-axis microscope and are colour-coded by the number of reflections detected at that data-collection site in the well (Fig. 2*f*). Crystals that have been shot are usually visibly damaged (Figs. 2*g* and 2*h*).

2.2.3. Data collection: IMISX at room temperature. IMISX diffraction data collection was carried out at hutch temperature (~20°C) with 10 × 10, 10 × 18 or 10 × 30 µm X-ray microbeams providing 1.5 × 10^{11}, 3 × 10^{11} or 1.5 × 10^{12} photons s^{-1}, respectively, at 12.0 keV (1.0332 Å) on beamline PX II (X10SA) at the Swiss Light Source, Villigen, Switzerland. Measurements were made in steps of 0.1–0.2° at speeds of 1–4 deg s^{-1} using a Pilatus 6M-F detector operated in shutterless mode at a frame rate of 10–20 Hz and at a sample-to-detector distance of between 20 and 60 cm. The X-ray wavelength and beam transmission that were used in data collection for native lysozyme, $PepT_{St}$ and AlgE were 1.0332 Å (12.0 keV) and 10–100%, respectively. For bromine SAD and sulfur SAD measurements, data were collected using 0.9205 Å (bromine absorption *K*-edge) and 1.7 Å

Table 1
Data-collection and refinement statistics for lysozyme.

Except for CC_{anom}, all data-processing statistics are reported with Friedel pairs merged. Values in parentheses are for the highest resolution shell.

	Lyso-Native	Lyso-Br	Lyso-S	Lyso-Native	Lyso-Br	Lyso-S
PDB code	4xjd	4xjg	4xji	4xjb	4xjf	4xjh
Data collection						
Temperature (K)	100	100	100	293	293	293
Presentation	Loop	Loop	Loop	*In situ*	*In situ*	*In situ*
Phasing method	MR	Bromine SAD	Sulfur SAD	MR	Bromine SAD	Sulfur SAD
Space group	$P4_32_12$	$P4_32_12$	$P4_32_12$	$P4_32_12$	$P4_32_12$	$P4_32_12$
Unit-cell parameters						
a (Å)	77.51	78.39	78.71	79.09	79.10	79.10
b (Å)	77.51	78.39	78.71	79.09	79.10	79.10
c (Å)	36.75	37.88	37.33	38.29	38.47	38.24
$\alpha = \beta = \gamma$ (°)	90	90	90	90	90	90
Unit-cell volume (Å^3)	220787	232772	231269	239513	240699	239260
Wavelength (Å)	1.0332	0.9194	1.7	1.0332	0.9205	1.7
No. of crystals	1	1	3	113	239	992
Resolution (Å)	50–1.80 (1.91–1.80)	50–1.80 (1.91–1.80)	50–2.0 (2.11–2.0)	50–1.80 (1.91–1.80)	50–1.80 (1.91–1.80)	50–2.00 (2.11–2.00)
R_{meas}	0.108 (0.873)	0.352 (1.482)	0.093 (0.273)	0.257 (0.756)	0.227 (1.409)	0.138 (0.562)
$R_{p.i.m.}$†	0.041 (0.320)	0.049 (0.225)	0.012 (0.041)	0.091 (0.271)	0.040 (0.245)	0.014 (0.080)
$\langle I/\sigma(I)\rangle$	12.0 (1.9)	12.8 (2.8)	48.0 (17.0)	5.5 (2.2)	12.9 (3.3)	45.0 (15.1)
Completeness (%)	99.6 (99.1)	100 (100)	100 (100)	99.7 (99.5)	99.9 (99.9)	99.8 (99.4)
Multiplicity	7.0 (7.0)	49.7 (43.6)	65.0 (44.9)	8.0 (7.8)	32.3 (33.2)	102.5 (49.3)
$CC_{1/2}$	0.99 (0.72)	1.00 (0.40)	1.00 (0.99)	0.98 (0.75)	1.00 (0.86)	1.00 (0.99)
CC_{anom}‡	—	0.65	0.47	—	0.48	0.41
Mosaicity§ (°)	0.16	0.17	0.12	0.06	0.04	0.05
Refinement						
Resolution (Å)	34.66–1.80	39.20–1.80	39.36–2.00	39.55–1.80	39.55–1.80	39.36–2.00
No. of reflections	10805	11423	8357	11703	11796	8346
R_{work}/R_{free}	0.22/0.27	0.20/0.24	0.16/0.21	0.17/0.21	0.18/0.21	0.16/0.20
No. of atoms						
Protein	1000	1000	1000	1015	1016	1016
Ligand/ion	8	6	9	6	6	6
Water	43	94	96	49	51	54
B factors (Å^2)						
Protein	28.89	18.19	18.89	28.75	24.57	26.61
Ligand/ion	37.38	24.54	36.14	36.62	39.94	33.10
Water	31.37	23.03	23.32	36.11	31.18	31.70
R.m.s. deviations						
Bond lengths (Å)	0.007	0.007	0.007	0.007	0.007	0.007
Bond angles (°)	1.052	1.014	1.018	1.108	1.089	1.018
Ramachandran plot						
Favoured (%)	98.43	98.43	98.43	99.23	98.46	98.45
Allowed (%)	1.57	1.57	1.57	0.77	1.54	1.55
Outliers (%)	0	0	0	0	0	0
MolProbity clashscore	7.12	2.04	1.53	2.01	2.49	4.49

† $R_{p.i.m.}$ was calculated as $R_{meas}/(\text{multiplicity})^{1/2}$. ‡ Anomalous correlation coefficient evaluated with data truncated to 2.5 Å resolution. § For IMISX data, the mosaicity is reported as the median over all crystals.

X-rays, respectively, at a speed of 1 deg s^{-1} with 3–10% transmission.

2.2.4. Data collection: harvested at 100 K. For reference, data were collected from crystals that had been grown *in meso* and that were harvested and snap-cooled in liquid nitrogen by conventional methods. For this purpose, the COC plates were opened with a scalpel to expose the mesophase. A 20–50 µm cryo-loop was used to retrieve the crystal or crystals from the bolus, with as little adhering mesophase as possible, and was immediately snap-cooled in liquid nitrogen without added cryoprotectant. The loops were stored in Dewars and shipped to the SLS for data collection.

2.2.5. Radiation damage at room temperature. To characterize radiation damage, an EIGER 1M detector (Dinapoli *et al.*, 2011) was used to collect sets of still diffraction images from lysozyme crystals in IMISX plates at room temperature. The EIGER is a single photon-counting and readout noise-free detector and features frame rates to 3 kHz, readout times to 3 µs and a pixel size of 75 µm. In this study, a frame rate of 500 Hz (2 ms per image) and a readout time of 20 µs were used. A total of 500 still diffraction images were collected from each lysozyme crystal with a 10 × 50 µm sized unattenuated beam. Nine and ten crystals were employed for data collection at wavelengths of 1.7 and 1.0332 Å with estimated dose rates of 1.5 and 3.3 MGy s^{-1}, respectively (Supplementary Table S1 and Supplementary Movie).

2.2.6. Data processing and merging. All 'conventional cryo-data' from samples in loops at 100 K were processed with *XDS* and scaled with *XSCALE*.

SX diffraction data were processed using scripts that automatically ran *XDS* for each data set. These scripts implemented a few tuning measures to deal with very sharp

Table 2
Data-collection and refinement statistics for $PepT_{St}$ and AlgE.

All data-processing statistics are reported with Friedel pairs merged. Values in parentheses are for the highest resolution shell.

	$PepT_{St}$	$PepT_{St}$	AlgE	AlgE
PDB code	4xnj	4xni	4xnl	4xnk
Data collection				
Temperature (K)	100	293	100	293
Sample treatment	Loop	*In situ*	Loop	*In situ*
Space group	$C222_1$	$C222_1$	$P2_12_12_1$	$P2_12_12_1$
Unit-cell parameters				
a (Å)	102.88	106.88	47.38	48.01
b (Å)	110.16	114.61	73.12	74.34
c (Å)	110.96	111.13	184.84	184.69
$\alpha = \beta = \gamma$ (°)	90	90	90	90
Unit-cell volume (Å^3)	1257539	1361289	640364	659170
Wavelength (Å)	1.03313	1.03319	1.03321	1.03318
No. of crystals	1	572	1	175
Resolution (Å)	50–2.30 (2.44–2.30)	50–2.80 (2.87–2.80)	50–2.90 (3.06–2.90)	50–2.80 (2.90–2.80)
R_{meas}	0.121 (1.106)	0.412 (1.673)	0.375 (2.037)	0.318 (1.116)
$R_{p.i.m.}$†	0.058 (0.533)	0.130 (0.534)	0.175 1.030)	0.134 (0.478)
$\langle I/\sigma(I)\rangle$	9.4 (1.3)	4.0 (1.1)	5.5 (1.2)	4.0 (1.1)
Completeness (%)	99.2 (97.2)	99.9 (99.8)	96.5 (99.0)	94.3 (96.0)
Multiplicity	4.4 (4.3)	10.1 (9.8)	4.6 (4.6)	5.6 (5.4)
$CC_{1/2}$	0.99 (0.59)	0.98 (0.49)	0.99 (0.43)	0.98 (0.57)
Mosaicity‡ (°)	0.07	0.05	0.36	0.07
Refinement				
Resolution (Å)	49.34–2.30	48.16–2.80	47.12–2.90	47.42–2.80
No. of reflections	28208	17118	14392	16066
R_{work}/R_{free}	0.20/0.25	0.21/0.24	0.25/0.29	0.23/0.27
No. of atoms				
Protein	3613	3450	3377	3347
Ligand/ion	291	225	230	95
Water	53	16	28	26
B factors (Å^2)				
Protein	53.41	78.54	53.66	51.89
Ligand/ion	67.09	99.20	60.41	74.61
Water	46.95	78.21	40.58	49.50
R.m.s. deviations				
Bond lengths (Å)	0.007	0.009	0.008	0.008
Bond angles (°)	1.182	1.314	1.09	1.07
Ramachandran plot				
Favoured (%)	98.48	96.6	94.3	94.7
Allowed (%)	1.52	3.4	5.5	4.8
Outliers (%)	0	0	0.2	0.5
MolProbity clashscore	7.30	6.22	4.63	2.38

† $R_{p.i.m.}$ was calculated as $R_{meas}/(\text{multiplicity})^{1/2}$. ‡ For IMISX data, the mosaicity is reported as the median over all crystals.

reflections and partial data sets. On the PILATUS detector, which has a zero point-spread function, many reflections were recorded on only a single pixel for measurements made at room temperature, where the mosaicity was typically much less than 0.1°. We used the keyword `MINIMUM_NUMBER_OF_PIXELS_IN_A_SPOT=1` in order to optimize the spot-finding step *COLSPOT* in *XDS*. All collected reflections were used for indexing with the known unit-cell parameters. Reflection intensities on each frame were then integrated with the keywords `CORRECTIONS=""` and `MINIMUM_I/SIGMA=50` to prevent *XDS* from scaling the intensities and adjusting the sigmas.

XSCALE was used to scale and merge the partial data sets. All reflections with a partiality of greater than 75% (the *XDS* default) were included in the final data set. If there were data sets which had only a few reflections in common with other data sets, *XSCALE* stopped with an error message. In such cases, a custom program was used to calculate, from the unscaled data sets themselves, an internal reference data set to stabilize the *XSCALE* calculation. This custom program writes out the median of the unscaled intensities of each observation as a robust but inaccurate estimate of its intensity. It also serves to identify a situation in which a group of data sets does not have common reflections with any other group of data sets. In this case, the smallest group of data sets that does not overlap with the rest of the data must be omitted from the *XSCALE* calculations because the relative scaling of two non-overlapping groups of data sets cannot be found. To validate this scaling approach, we also tried using complete experimental data sets collected at cryogenic temperature or squared F_{calc} values from a structure model as reference data sets. However, we found that the origin of the reference data set had little influence on the resulting scaled data. Since the median-scaled reference data set can be calculated in any situation, we routinely used it for the first *XSCALE* iteration and subsequently replaced it with the resulting scaled data set.

Non-isomorphous data sets were rejected in an iterative procedure. In each iteration, the statistics (in particular $CC_{1/2}$ and completeness) of the isomorphous and the anomalous signal were monitored, and the data sets with the lowest $I/\sigma_{asymptotic}$ value (Diederichs, 2010) were identified. These data sets (at most 1% of the total number) were omitted in the next iteration. Iterations were stopped when $CC_{1/2}$ no longer rose or the completeness started to drop. We found that the success of the downstream calculations did not depend on the exact number of rejection iterations. Data-collection and processing statistics are provided in Tables 1 and 2.

2.2.7. Structure determination and refinement. Molecular replacement (MR) was used to search for a solution in the native lysozyme, $PepT_{St}$ and AlgE data sets using *Phaser* (McCoy *et al.*, 2007) with PDB entries 3tmu (Kmetko *et al.*, 2011), 4d2b (Lyons *et al.*, 2014) and 4afk (Tan *et al.*, 2014) as the model templates, respectively. The single-wavelength

anomalous diffraction (SAD) method was employed for experimental phasing using anomalous diffraction data sets from native (Lyso-S) and bromine-derivative lysozyme (Lyso-Br) crystals. Heavy-atom locations, structure phasing and density modification were obtained using the *HKL2MAP* interface to *SHELXC*, *SHELXD* and *SHELXE* (Sheldrick, 2010). Heavy-atom substructures of Lyso-S and Lyso-Br were identified with 1000 *SHELXD* trials, and initial phasing employed 20 cycles of *SHELXE* density modification with autobuilding of the protein backbone trace. The model was completed using *Coot* (Emsley & Cowtan, 2004). *PHENIX* (Adams *et al.*, 2002) and *BUSTER* (Bricogne, 1993; Roversi *et al.*, 2000) were used during the refinement of all structures, with the 'strategy' options of 'individual sites', 'real space', 'individual atomic displacement parameter', 'ordered solvent' and 'target weight optimization' turned on. The refinement statistics are reported in Tables 1 and 2. The figures were generated with *PyMOL* (http://www.pymol.org).

All diffraction data and refined models have been deposited in the Protein Data Bank as entries 4xjd, 4xjg, 4xji, 4xjb, 4xjf, 4xjh, 4xnj, 4xni, 4xnl and 4xnk.

3. Results

3.1. IMISX plates

Given the importance of plate functionality in the proposed SX measurements, issues relating to the properties and performance of the plates will be dealt with ahead of the diffraction measurements. IMISX plates were designed for use both manually and with a robot, as has been implemented with standard *in meso* crystallization plates (Cherezov *et al.*, 2004). The bulk of the work reported here was performed with a robot, and three different commercial robots were evaluated (§2). All performed equally well with the new plates. The IMISX plates could be filled, sealed and handled with the same ease as standard glass plates. Interestingly, treating the COC film with silanizing agent was found to be important for effective mesophase delivery to wells despite the fact that the copolymer was not expected to react chemically with the reagent. Plates could be stored in the incubator/imaging device and imaged reliably with a microscope under bright-field and polarized light (§2), as for standard plates (Supplementary Figs. S2*b* and S2*c*). Given the UV transparency of the COC film and the fact that the windows together are only 50 µm thick, UV imaging, *via* tryptophan fluorescence, can be used as a means of evaluating whether or not a crystal is proteinaceous (Supplementary Figs. S2*a* and S2*d*), assuming that the target protein has a measurable complement of tryptophans.

The conditions that gave rise to crystals with standard glass plates translated almost exactly to the IMISX plates for all of the proteins included in this study. Indeed, for some targets the same hit rate and crystal size and frequency were observed with the two plate types.

As assembled, the new double-sandwich plates proved to be quite watertight, a property of the original *in meso* glass plates that we set out to replicate in the new design. Specifically, an ∼5% change in the liquid mass of a filled 96-well double-sandwich IMISX plate was recorded over 25 d at 20°C, which is similar to the water loss observed with standard glass plates (Supplementary Fig. S1; Cherezov & Caffrey, 2003). By comparison, similar measurements made with isolated exposed COC plates revealed a loss of ∼75% of the liquid mass in the same period (Supplementary Fig. S1).

Because the optical transparency of the IMISX plates is close to that observed with standard *in meso* plates, crystals that are just micrometres in size can be seen readily using a light microscope. This greatly facilitates the identification of initial crystallization hits and tracking crystal growth either by hand or automatically in an incubator–imager. It is also important for efficiently identifying and centring, with the on-axis microscope at the synchrotron beamline, crystals and their coordinates in the mesophase bolus for use in automated SX (Fig. 2*f*).

The IMISX plates are of slim design, in part to reduce X-ray scattering and absorption. At a total thickness of 50 µm, the two COC windows through which the X-rays pass in the process of *in situ* measurements contribute relatively little to background scattering and absorption (Supplementary Figs. S3*c* and S3*e*). Because COC scattering is weak and diffuse, with a maximum centred at around 5 Å, it is not a major problem as far as current crystal diffraction measurements are concerned. Likewise, absorption is not an issue. The calculated X-ray attenuation for 50 µm COC is <3% at 0.9205, 1.0332 and 1.7 Å (Henke *et al.*, 1993), the three wavelengths used in this study. In contrast to the window material of the IMISX plates, mesophase absorption and low-angle scattering are stronger. In part, this is owing to the thickness of the bolus, which ranged nominally from 64 to 140 µm, and to the fact that the mesophase, a liquid crystal, scatters strongly at both low and wide angles. Scattering is typically powder-type. In the low-angle region, it extends as a series of sharp, spotty rings out to about 20 Å resolution. At wide angles, scattering is diffuse and is centred at ∼4.6 Å resolution. It overlaps with that from the COC. Both regions of scattering contribute to decreasing the crystal diffraction signal to noise. Efforts were made to reduce the background from the sample by working with thinner mesophase boluses. The bulk of the measurements were made with samples that were 140 µm thick. However, for the more demanding membrane-protein crystals and for SAD measurements, data were collected using samples that were 64 µm thick. Attempts were made to use 50 µm spacers to give even thinner samples. These failed, however. The corresponding plates were very difficult to assemble and to handle reproducibly and the conditions under which crystals grew were different from those observed with standard glass plates.

As double-sandwich plates, the IMISX plates proved to be extremely robust and could be handled and shipped with ease. After opening and COC plate removal, the latter are typically reinforced with a rigid plastic backing to facilitate handling and mounting on the goniometer for use in data collection. Sections of the COC plate that are not required for immediate

use are returned and sealed in the original glass plate for long-term storage at 20°C.

3.2. Lysozyme

Lysozyme was chosen as the test protein with which to develop and evaluate the IMISX method for several reasons. To begin with, it produces crystals that diffract to high resolution under standard *in meso* conditions. A protocol is available for producing crystals *in meso* within 1 h (Aherne *et al.*, 2012). *In meso*, the enzyme crystallizes in space group $P4_32_12$, for which only 90° of data are needed for a complete data set. *In meso* crystals of lysozyme tend to be small (10–30 µm) and thus nicely mimic those obtained with typical membrane proteins. Lysozyme can be heavy atom-labelled with ease and has ten S atoms (two Met and eight Cys residues in a total of 129). As a result, it can be used to evaluate the IMISX method for native and heavy-atom phasing. Lysozyme has been employed as a test protein in many applications and much is known about its crystallographic behaviour at 100 K and at RT and of its sensitivity to X-rays. For these reasons, it was considered an ideal test case, where the lessons learned using it would apply directly to the more challenging membrane proteins that come at a premium.

3.2.1. Native lysozyme: molecular-replacement phasing. IMISX plates were set up with lysozyme as outlined in §2. Crystals grew within 1 h and were considered to have reached a size (20 µm) suitable for data collection after 6 h at RT (Fig. 2*b*). For reference, crystals were harvested from the IMISX plates with cryo-loops, snap-cooled in liquid nitrogen and used for data collection at 100 K. Phasing was performed by MR with PDB entry 3tmu as the model. Data-collection and refinement statistics for these snap-cooled crystals are presented in Table 1. The crystals, which belonged to space

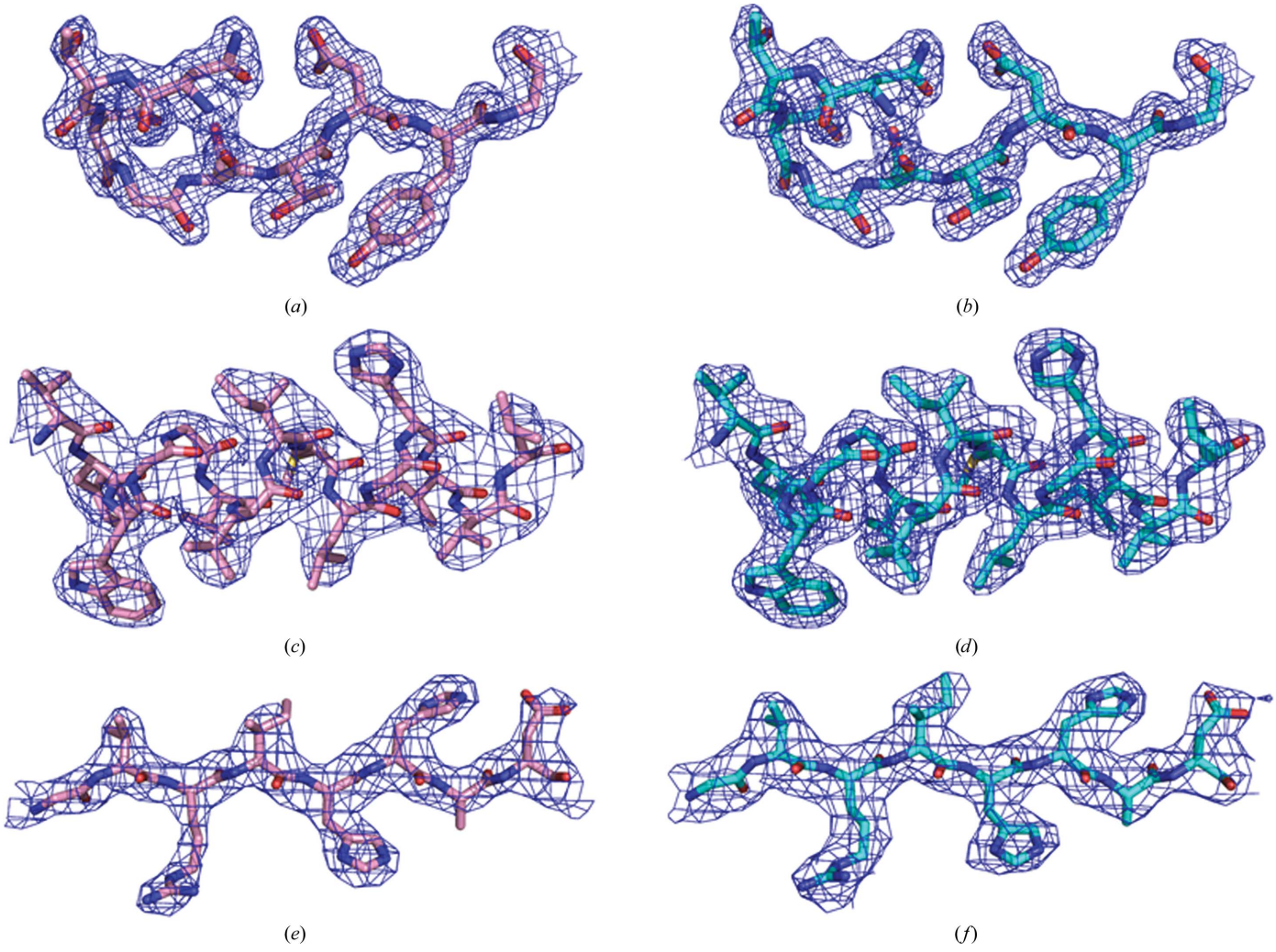

Figure 3
A comparison of electron-density maps for measurements made by the IMISX method at room temperature (*a*, *c*, *e*) and by the conventional method using harvested crystals at 100 K (*b*, *d*, *f*) for lysozyme (*a*, *b*), $PepT_{St}$ (*c*, *d*) and AlgE (*e*, *f*). Residues Asn46–Gly54, Val88–Leu102 and Gly222–Asp229 are shown for lysozyme, $PepT_{St}$ and AlgE, respectively. The $2F_o - F_c$ maps are shown as blue meshes contoured at 1σ. The resolution of the corresponding data are 1.8, 2.8 and 2.8 Å for lysozyme, $PepT_{St}$ and AlgE at room temperature, respectively. At 100 K, the corresponding resolution values are 1.8, 2.3 and 2.9 Å, respectively. Stick models show N atoms (blue), O atoms (red) and C atoms (pink at room temperature, light blue at 100 K).

group $P4_32_12$, diffracted to 1.8 Å resolution with a completeness of 99.1%, a $CC_{1/2}$ of 0.72 and an $\langle I/\sigma(I)\rangle$ of 1.9 in the highest resolution shell. The structure was refined with an R_{work} and an R_{free} of 0.22 and 0.27, respectively (Table 1).

IMISX data were collected using crystals from the same or similar plates to those used for reference data collection at 100 K. Specifically, 113 crystals from two wells were used for structure determination. The crystals had average dimensions of 10 × 10 × 20 µm. For each crystal, a total of 2° of data were collected in 0.2° and 0.05 s wedges with a 10 × 18 µm beam at 3×10^{11} photons s^{-1}. Because of radiation damage, only the first 1.2° of data were actually used for structure solution by MR and refinement. In the highest resolution shell, the completeness was 99.5%, the $CC_{1/2}$ was 0.75 and $\langle I/\sigma(I)\rangle$ was 2.2. The structure was refined to a resolution of 1.8 Å with an R_{work} and R_{free} of 0.17 and 0.21, respectively (Table 1). The corresponding electron-density map is of high quality and the model is virtually identical [backbone root-mean-square deviation (r.m.s.d.) of 0.257 Å over 129 residues] to that obtained from crystals at 100 K (Figs. 3*a* and 3*b*). The maps revealed the presence of several chloride ions, as expected, and a sodium ion octahedrally coordinated by the backbone carbonyl O atoms of Ser60, Cys64 and Arg73, the O^{γ} atom of Ser72 and two water molecules (Supplementary Fig. S5). This result demonstrates convincingly that the IMISX method works with lysozyme crystals. Given the close to 100%

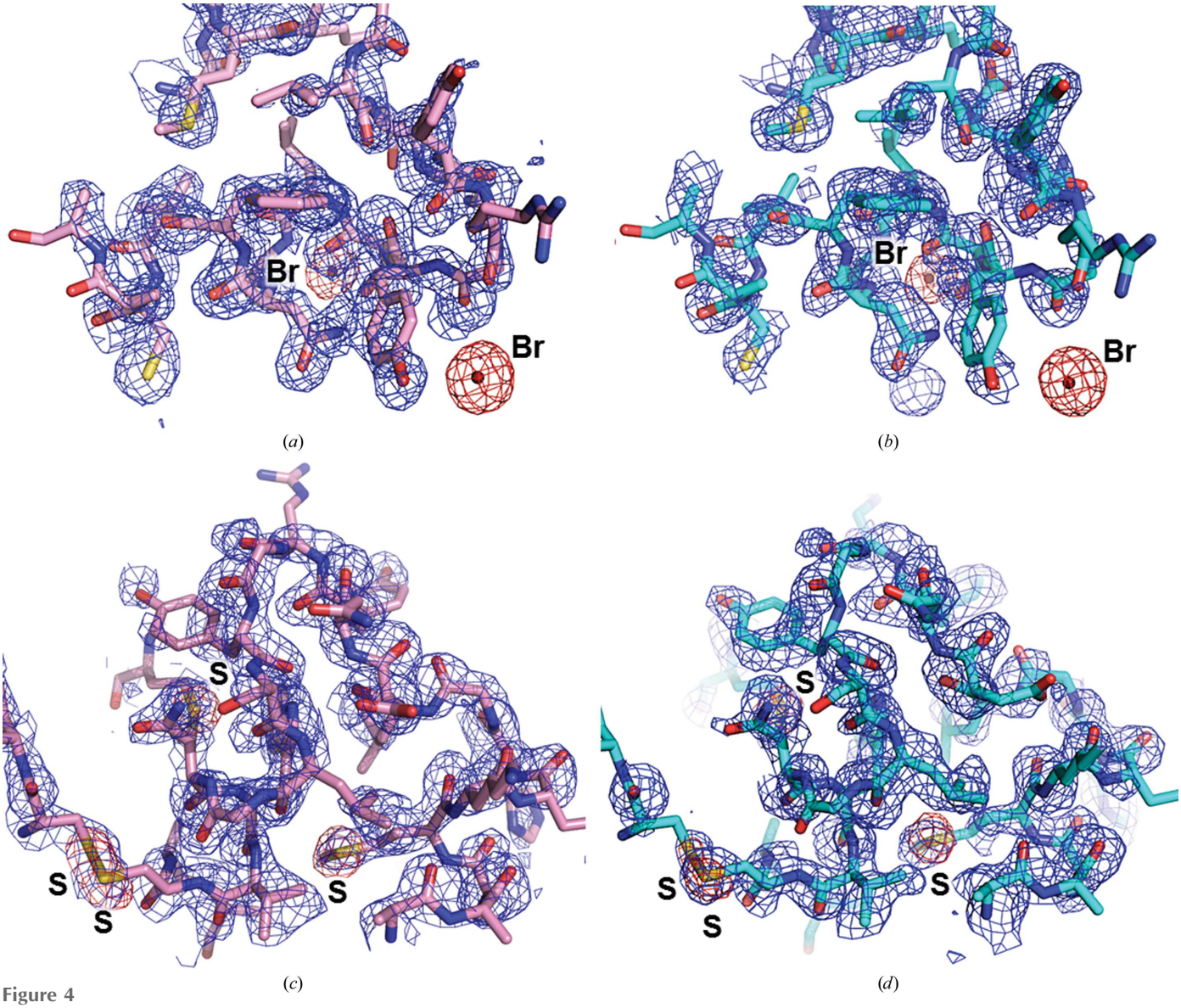

Figure 4
A comparison of the initial electron-density maps obtained by bromine SAD (*a*, *b*) and sulfur SAD (*c*, *d*) phasing for measurements made with lysozyme by the IMISX method at room temperature (*a*, *c*) and by the conventional method using harvested crystals in loops at 100 K (*b*, *d*). Residues Ala9–Ala32 are shown for the bromine SAD data (*a*, *b*) and residues Ala9–Ala32, Met105, Cys115 and Lys116 for the sulfur SAD data. The initial $2F_o - F_c$ map obtained after density modification with *SHELXE* was contoured at 1σ and is shown as a blue mesh. The anomalous difference maps contoured at 5σ are shown as a red mesh. Br and S atoms are labelled. The final model is shown in stick representation. The resolutions of the corresponding data are 2.0 and 1.8 Å for sulfur SAD and bromine SAD at room temperature, respectively. At 100 K, the corresponding values are 2.0 and 1.8 Å, respectively.

completeness, the crystals are clearly oriented randomly in the LCP. For purposes of IMISX data collection, two boluses of mesophase were used corresponding to 400 nl mesophase, 240 nl lipid and 8 µg protein (Supplementary Table S2).

3.2.2. Lysozyme: bromine SAD phasing. MR phasing worked well for data collected from native lysozyme crystals using the IMISX method. The next objective was to evaluate the utility of the method with experimental phasing. Initial tests were performed with lysozyme crystals grown *in meso* in the presence of NaBr. This introduces bromide ions into the crystal lattice that can be used for SAD phasing. The crystals grown in this way were relatively large, with dimensions of at least 10 × 20 × 30 µm (Fig. 2*c*). A reference cryo-structure was solved to a resolution of 1.8 Å with diffraction data collected at 13.485 keV (0.9194 Å), the bromine X-ray absorption edge energy, using a single crystal harvested from mesophase in an IMISX plate. The corresponding IMISX data were recorded and analyzed in a similar fashion but with the samples held at RT. In this case, a total of 279 crystals in four wells were measured and 239 crystals were used for structure determination. Data collection consisted of recording 2° of data from each crystal in wedges of 0.1° at 1 deg s^{-1} with a 10 × 18 µm beam at 1.5 × 10^{10} photons s^{-1}. A total of 4780 diffraction images made up the final data set. In the highest resolution shell, the completeness was 99.9%, the $CC_{1/2}$ was 0.86 and $\langle I/\sigma(I)\rangle$ was 3.3. The structure was solved by SAD phasing with CC_{all} and CC_{weak} of 33.4 and 16.1, respectively, in *SHELXD* and a well separated contrast between the correct and inverted hands in *SHELXE* (Supplementary Fig. S4*a*). The structure was refined to a resolution of 1.8 Å with an R_{work} and an R_{free} of 0.18 and 0.21, respectively (Table 1). The electron-density maps and the models obtained for both types of data are very similar, with a backbone r.m.s.d. value of 0.169 Å over 129 residues. The anomalous difference map contoured at 5σ shows five well defined lobes of density attributed to bromide ions in both the IMISX and the 100 K data (Figs. 4*a* and 4*b*; Supplementary Fig. S5*b*). The bromide locations are isomorphous with chlorides and bromides in published lysozyme structures (chloride, PDB entries 1gwd, 2w1l, 2w1y, 2w1x, 2w1m, 4a7d, 2xoa, 2xbs, 2xbr, 2xjw, 1w6z and 4aga; bromide, PDB entry 1azf), which typically contain from three to nine halides. For the purposes of obtaining this bromine SAD structure by the IMISX method, 800 nl mesophase representing 16 µg protein and 480 nl 9.9 MAG was used (Supplementary Table S2). These results show that bromine SAD is possible by the IMISX method as applied to lysozyme crystals. The anomalous signal from bromine is similar to that from selenium. Thus, while selenium-labelled protein was not used in this study, the results obtained with bromine SAD suggest that selenium SAD phasing should be possible using IMISX.

3.2.3. Lysozyme: sulfur SAD phasing. Bromine SAD phasing worked well. The question we next sought to answer was: will IMISX work for the considerably more challenging native sulfur SAD? Once again, lysozyme provided a good test protein because ten of its 129 residues contain sulfur. Nonetheless, with native SAD phasing the anomalous signal is weak and data collection must be optimized to obtain the best possible signal-to-noise ratio. In this case, diffraction data were collected at an X-ray wavelength of 1.7 Å, where the sulfur f'' is 0.67 electrons. A reference data set was recorded from three single crystals at 100 K that had been harvested from an IMISX plate with crystals grown at 20°C. The IMISX measurements were made on 1290 crystals in 12 wells, of which 992 provided useful data. Data were collected with a 10 × 30 µm beam at 9 × 10^9 photons s^{-1}. In the highest resolution shell, the completeness values were 100 and 99.4%, the $CC_{1/2}$ values were 0.99 and 0.99, and the $\langle I/\sigma(I)\rangle$ values were 17.0 and 15.1 for the 100 K and IMISX data, respectively. The structures of the 100 K and IMISX crystals were solved by sulfur SAD phasing with CC_{all}/CC_{weak} of 37.0/20.4 and 39.0/21.6 in *SHELXD*, respectively (Supplementary Figs. S4*c* and S4*d*). Structures were refined to resolutions of 2.00 and 2.00 Å and with R_{work}/R_{free} values of 0.16/0.21 and 0.16/0.20, respectively (Table 1). The anomalous difference maps contoured at 5σ show 14 and 11 well defined lobes corresponding to ten and ten S atoms and four and one chloride ions for the 100 K and IMISX data, respectively (Figs. 4*c* and 4*d*). The quality of the electron-density maps for both sets of samples is extremely high and the models are very similar (backbone r.m.s.d. of 0.196 Å over 129 residues; Supplementary Fig. S5*c*). For the purposes of obtaining this sulfur SAD structure by the IMISX method, 2400 nl mesophase representing 48 µg protein and 1440 nl 9.9 MAG was used (Supplementary Table S2). These data show clearly that native sulfur SAD works with IMISX as applied to crystals of lysozyme.

3.3. $PepT_{St}$

Thus far, the IMISX method has been shown to work well with the test protein lysozyme. Our next task was to evaluate its usefulness with a protein for which IMISX was designed, an integral membrane protein. Two were chosen, the first of which was $PepT_{St}$, an α-helical peptide transporter (53 kDa) from *S. thermophilus*. $PepT_{St}$ is a good model membrane protein. It is relatively easy to produce with high purity and in good yield, it is stable on storage and crystals grow quickly and reproducibly *in meso* at RT. *In meso* crystals are blocky, highly birefringent and easy to observe growing in the cubic phase (Fig. 2*d*). Further, the crystals diffract well and structures of the protein alone and in complex with peptides have been solved to better than 2.4 Å resolution (Lyons *et al.*, 2014). $PepT_{St}$ crystals grow optimally in 7.8 MAG, which is a short-chain variant of the standard host lipid 9.9 MAG. This then provided an opportunity to evaluate the IMISX method with a material whose mesophase and rheological properties are somewhat different from those of the reference MAG. At the same time, it is representative of other short-chain MAGs that are growing in popularity for *in meso* crystallogenesis (Caffrey, 2015).

Reference diffraction measurements were made at 100 K with a crystal of $PepT_{St}$ harvested directly from an IMISX plate. $PepT_{St}$ crystallized in space group $C222_1$. The crystals diffracted to 2.3 Å resolution, where the highest resolution

shell had a completeness of 97.2%, a $CC_{1/2}$ value of 0.59 and an $\langle I/\sigma(I)\rangle$ of 1.3 (Table 2). For IMISX measurements, 20 wells were interrogated, representing 1363 crystals with an average size of 10 × 10 × 20 µm (Fig. 2*d*). Of these, 1101 crystals were used for data collection covering 1–2° with 0.1° and 0.1 s wedges with a 10 × 18 µm beam at 7.5×10^{10} photons s^{-1}. The remainder of the data were collected in wedges of 0.2° and 0.05 s with a 10 × 18 µm beam at 3×10^{11} photons s^{-1}. Useful diffraction data were obtained from 572 crystals, where the processed data included the first 0.6° of coverage. The corresponding structure was solved to a resolution of 2.8 Å in space group $C222_1$. The highest resolution shell had a completeness of 99.8%, a $CC_{1/2}$ value of 0.49 and an $\langle I/\sigma(I)\rangle$ of 1.1. The electron densities and molecular models of the 100 K and IMISX structures are remarkably similar (backbone r.m.s.d. of 0.463 Å over 463 residues; Supplementary Figs. S6*a* and S6*b*). The quality of the electron density for both is remarkably high (Figs. 3*c* and 3*d*). For IMISX data collection, 1320 nl mesophase representing 660 nl 7.8 MAG and 6.6 µg protein was used (Supplementary Table S2).

3.4. AlgE

The second integral membrane protein used to evaluate the IMISX method was AlgE, the alginate transporter (54 kDa) from *P. aeruginosa*. By contrast with $PepT_{St}$, AlgE is a β-barrel protein. It facilitates the movement of alginate, an important component of the biofilm, across the outer membrane of this opportunistic human pathogen. The protein was a good test case for many of the same reasons as listed above for $PepT_{St}$. It is stable, available in relatively large amounts and crystallizes *in meso* in 7.8 MAG at RT. Further, several structures of the protein have been solved in different conformational states, the best to a resolution of 1.90 Å (Tan *et al.*, 2014).

A reference data set was collected at 100 K from a crystal of AlgE harvested from an IMISX plate, providing a structure to 2.90 Å resolution in space group $P2_12_12_1$. The highest resolution shell had a completeness of 99.0%, a $CC_{1/2}$ value of 0.43 and an $\langle I/\sigma(I)\rangle$ of 1.2. For IMISX, one well was examined, representing 484 crystal measurements (some needle-shaped crystals were long enough to be interrogated at up to three locations along the crystal) with average dimensions of 5 × 5 × 30 µm (Fig. 2*e*), and the final data set was merged with data from 175 crystals. Data were collected with a 10 × 10 µm beam at 1.5×10^{11} photons s^{-1}. The structure was solved to a resolution of 2.8 Å in space group $P2_12_12_1$. The highest resolution shell had a completeness of 96.0%, a $CC_{1/2}$ value of 0.57 and an $\langle I/\sigma(I)\rangle$ of 1.1 (Table 2). The molecular models of the 100 K and IMISX structures are very similar for all of the protein except loops 5 and 6 (L5 and L6) and β-strands 11 and 12 (S11 and S12), as discussed below (§3.5; Supplementary Fig. S7). Omitting L5 and L6, the backbone r.m.s.d. was 0.461 Å over 417 residues. The quality of the electron density for both is remarkably high (Figs. 3*e* and 3*f*). For AlgE IMISX data collection and structure solution, 50 nl mesophase representing 25 nl 7.8 MAG and 0.25 µg protein was used (Supplementary Table S2).

3.5. Cryo *versus* room-temperature (harvested *versus in situ*) structures

For the proteins included in this study, measurements were made on crystals *in situ* at room temperature and, for reference, on crystals harvested in loops at 100 K. The crystals used came from adjacent wells on the same plate and were grown using the one precipitant at 20°C. With the exception of temperature, diffraction measurements were made under conditions that were as similar as possible. Assuming that the harvesting and snap-cooling processes are benign, differences in structure between the *in situ* and cryo models are attributed to temperature.

The differences observed for all three lysozyme structure types (Lyso-Native, Lyso-Br and Lyso-S) as a function of data-collection temperature are remarkably few (Supplementary Table S3*a*). As expected, the unit-cell volumes are larger in all cases at the higher temperature. The minimum and maximum increases observed in unit-cell dimensions were 3.4 and 8.5%, respectively. Thermal expansion of this type has been reported previously (Tilton *et al.*, 1992; Fraser *et al.*, 2011; Keedy *et al.*, 2014). The r.m.s.d. between *in situ* and cryo models for the backbone-atom positions over all 129 residues in lysozyme ranged from 0.169 to 0.257 Å. Differences were observed in the number of structured waters and ions (Table 1). However, no consistent trend as a function of temperature between the three structure types was apparent.

Room-temperature structures can reveal conformational subsets, especially for side chains, that are different from those adopted at 100 K. Within the lysozyme structure set, very few such differences were observed (Supplementary Table S3*a*). Arg112 is an example where two distinct conformers were modelled into well defined electron density, one at 100 K and another at RT (Supplementary Fig. S8).

A comparison of the *in situ* and cryo crystal data for $PepT_{St}$ shows that the unit-cell volume increased with temperature by 8.3%. This derives principally from the 4–5 Å change in the *a* and *b* unit-cell axis lengths, with very minor changes observed along the *c* axis. Overall, the structure of the transporter changed little with temperature. The r.m.s.d. for backbone-atom positions from Gly5 to Gly477 was 0.463 Å. Differences were observed in the number of structured lipids and water molecules and in the number of residues that could be reliably modelled into density (Table 2, Supplementary Table S3*b*). The periplasmic end of the protein was essentially identical between the two data sets. The same applies to the N-terminal half of the helices to the cytoplasmic side. However, some differences were noted for the C-terminal half, which has been reported to undergo movement during transport (Fowler *et al.*, 2015). Here, the helices were shorter, with the number of missing residues, including those in loops, increasing significantly at the higher temperature (Supplementary Fig. S6*c* and Supplementary Table S3*b*). Helix 11 (H11) has been reported to bend at Ser431 towards the peptide pocket upon binding

Ala-Phe, a dipeptide transported by $PepT_{St}$ (Lyons *et al.*, 2014). In the apo form of the protein at 100 K, H11 is straight. The RT form of $PepT_{St}$ described here has H11 bent to a degree intermediate between the liganded and apo states. Given the promiscuity of $PepT_{St}$, this slight bending might be accounted for by partial occupancy of the binding pocket by small molecules carried along during protein preparation and crystallization. Indeed, density for such adventitious materials is obvious in the RT and cryo forms of $PepT_{St}$ reported here (Supplementary Figs. S6*d* and S6*e*).

As for lysozyme and $PepT_{St}$, the RT and cryo crystal parameters and structures of AlgE are remarkably similar. The unit-cell volume increased by 2.9% with temperature, with much of the change being accounted for by slight increases in the *a* and *b* unit-cell axis lengths. The number of ordered lipid, detergent and water molecules was much reduced at RT. The r.m.s.d. for backbone-atom positions from Pro39 to Phe490 was 0.55 Å. Both models have missing residues. Their locations and numbers are quite similar. The structure differences depending on temperature are listed in Supplementary Table S3(*c*). The largest disparity between the two structures is in extracellular loops L5 (Asp230–Gly250), S11 (Leu272–Thr291), L6 (Val292–Arg297) and S12 (Ile298–Trp318). These are bent slightly more (by a few degrees) towards the barrel core at RT than at 100 K. Both loops are involved in crystal contacts in the two models, and consequently the changes noted are not likely to have a functional significance. The conformation recorded at both temperatures is of the 'open-in' type, as reported previously (PDB entry 4afk; Tan *et al.*, 2014).

3.6. Radiation damage

Unlike data collection with femtosecond pulses generated by an XFEL, radiation damage is unavoidable for MX measurements made using synchrotron sources. At room temperature, radiation damage is a complex and dynamic chemical and structural process involving X-ray-generated photoelectrons as agents of primary damage. They produce low-energy secondary electrons that contribute to chemical bond breakage and radical generation and diffusion. These, in turn, can lead to changes in crystal lattice dimensions and to crystal deformations such as cracking and melting (Owen *et al.*, 2012; Warkentin *et al.*, 2013). The X-ray beam profile, positional stability, dose rate, crystal solvent content and composition, and crystal-to-crystal variability play important roles in the manifestation of radiation damage (Leal *et al.*, 2013). With the very limited rotation range used for data collection in this IMISX work, the X-ray footprint on a crystal remains essentially unchanged. This makes spot-fading a suitable method for characterizing radiation damage. At the high dose rate of 1.5–3.3 MGy s^{-1} used here, it takes a few hundred milliseconds to reach a life dose (the accumulated dose that a crystal can endure; Holton, 2009) of 0.2–0.5 MGy (Supplementary Table S1). This means that radiation damage can be observed as it occurs by taking snapshots of diffraction images using a fast X-ray detector with a millisecond frame rate and a negligible readout time. Accordingly, a series of 500 consecutive, still diffraction images (2 ms per image) were collected from single lysozyme crystals in IMISX plates held stationary in the goniometer at room temperature. The radiation-induced rise in crystal mosaicity and/or crystal deformation can be observed from the diffraction images directly (Supplementary Fig. S9*a* and Supplementary Movie). The first diffraction images at '0 MGy' reveal just a few sharp Bragg spots that undoubtedly reflect the intrinsically low mosaicity of these lysozyme micro-crystals at room temperature. The number of reflections per image initially increases with accumulated dose and damage as mosaicity increases. This accounts for the peak in integrated reflection intensity per image with accumulated dose at ∼0.2 MGy (Supplementary Figs. S9*b* and S9*c*). Beyond ∼0.3–0.4 MGy, the integrated intensity falls off dramatically.

The plots in Supplementary Fig. S9 provide a rough estimate of life dose at room temperature in the IMISX setup. For lysozyme it is about 0.3 MGy, which is one to two orders of magnitude less than that at 100 K, as expected (Warkentin *et al.*, 2013). Estimated accumulated dose per crystal values are listed in Supplementary Table S1 (Holton, 2009). For all three proteins used in this study, evidence of radiation damage was obvious from the raw diffraction images and from the visual appearance of the crystals when the dose per crystal exceeded 0.3 MGy. For native data sets, only data with accumulated dose values up to 0.27 MGy per crystal were used in structure determination. For experimental bromine SAD and sulfur SAD phasing, the corresponding values were 0.14 and 0.08 MGy, respectively.

3.7. Local mesophase characterization by SAXS/WAXS

A feature of the IMISX plates is that they can be used with relative ease to gain information about the mesophase in which crystals grow. This can shed light on the mechanism of *in meso* crystallogenesis to provide a more rational approach to structure-grade crystal production. In the current study, the relevant information was obtained by recording the SAXS and WAXS of the mesophase at some distance from and directly surrounding the growing/suspended crystal. The SAXS/WAXS data provide definitive phase identification and microstructure characterization. A limited number of such measurements were made as part of the current investigation (Supplementary Figs. S3, S10 and S11). These show that the mesophase surrounding $PepT_{St}$ crystals in 7.8 MAG is of the sponge phase, with hints of the cubic phase at some distance from the crystal (Supplementary Fig. S11). A more detailed exploration of the hosting mesophase and how this relates to crystal growth, as has been performed previously (Cherezov & Caffrey, 2007), is beyond the scope of the current work. What these results show, however, is that such quantitative measurements are possible and that they can be performed essentially simultaneously with crystal diffraction data collection.

4. Discussion

4.1. Advantages of IMISX

In the following, the advantages of the IMISX method are discussed in no particular order of priority.

4.1.1. *In situ*. First and foremost, IMISX is an *in situ* measurement. It is performed directly in the environment and under the conditions in which the crystals grow. Data are collected with the protein the closest it can be to its native state while still being in a crystal lattice. *In situ* measurement is one of the most efficient routes, if not the most efficient route, to a final crystal structure. It represents immediate and unambiguous diffraction-quality evaluation, leading to informed optimization or, in the ideal case, directly to a structure. This is in contrast to other evaluation methods, which include visual inspection under a microscope with bright/dark-field or polarized light, UV and fluorescence microscopy, and second-order nonlinear optical imaging of chiral crystals (SONICC). These alternative methods must contend with issues relating to false positives, false negatives and, in certain cases, to an entire lack of signal. In contrast, with IMISX an initial hit consisting of a few or a shower of micro-crystals will usually provide, at the very least, a direct lead to optimization and, in the best cases, directly to a structure.

In situ, by its nature, means not needing harvesting. Harvesting small, fragile crystals from a viscous and sticky mesophase sealed in a glass sandwich plate is time-consuming, requires experience, skill and manual dexterity, and can damage the crystal, with consequences for data quality. It is particularly challenging in the case of thin, plate-like crystals that have weak or lack birefringence, where many crystals are lost in the process. IMISX avoids all of these problems.

IMISX is truly an *in situ* measurement. In this regard, it is unlike the other SX methods where, currently, the mesophase must be grown in one device (a coupled micro-syringe) and transferred to another (an LCP injector), from which it is extruded through a long, narrow-bore capillary under pressure, with severe limits on crystal size and sample homogeneity and cleanliness. Thus, crystals cannot exceed a given maximum size and the dispersion must be free of large aggregates, lint and dust. Otherwise, the injector fails owing to clogging. Further, LCP-SFX measurements that have been conducted at the Linac Coherent Light Source (LCLS) to date have been performed in an evacuated sample chamber. The high vacuum results in evaporative cooling of the mesophase, which can adversely affect sample delivery and damage the X-ray detector and delicate crystals suspended in the mesophase. An in-air SFX station equipped with a goniometer, as soon to be commissioned at the LCLS (Cohen *et al.*, 2014), should enable some of the advantages of the *in situ* plate introduced here to be exploited directly.

4.1.2. Miniscule sample consumption. IMISX measurements require extremely small quantities of valuable protein, lipid and, in the case of ligand screening, the ligand itself. As such, IMISX is likely to be one of the most efficient methods in terms of material overhead in going from the initial screen to the final structure. The statistics presented in §§3.2–3.4 (Supplementary Table S2) indicate that it is orders of magnitude more efficient than SFX as implemented at an FEL. In the current application, 250 ng AlgE and 6.6 µg $PepT_{St}$ were required for structure solution. By contrast, 220 µg DgkA, 500 µg serotonin receptor (5-HT_{2B}) and 300 µg smoothened receptor (SMO) were used for structure determination by the LCP-SFX method (Liu *et al.*, 2013; Weierstall *et al.*, 2014). The corresponding value for synchrotron SX *in meso* relates to bacteriorhodopsin, where 800 µg protein was required (Nogly *et al.*, 2015).

4.1.3. Small crystals. The IMISX method, as implemented here, works well with small crystals of the type typically formed under *in meso* conditions. These ranged in size from 10 to 30 µm in the maximum dimension. It is not unusual for initial hits to generate such crystals, which can be a challenge to harvest and snap-cool and to use for effective data collection at 100 K. Being able to employ them directly for *in situ* measurement is therefore a great advantage. Not needing to rescreen and optimize for larger crystals represents a major saving in time, materials and valuable resources.

SFX at an FEL is noted as a method that can work with very small crystals. Indeed, data leading to structures have been obtained with soluble protein crystals in aqueous suspension of just 3 µm in maximum dimension (Boutet *et al.*, 2012). With membrane proteins, the record is held by PS I, where crystals of about 1.4 µm suspended in an aqueous medium have yielded structures from interpretable electron-density maps (Chapman *et al.*, 2011). However, for SFX measurements on membrane-protein (DgkA, 5-HT_{2B} and SMO) crystals dispersed in the cubic phase, crystal sizes ranged from 5 to 20 µm (Liu *et al.*, 2013; Weierstall *et al.*, 2014; Caffrey *et al.*, 2014). It would appear therefore that IMISX, which generated structures of membrane proteins from crystals of 10–30 µm in size, compares favourably in this regard with extant SFX results.

4.1.4. Automation at synchrotron beamlines. The small format of the *in situ* COC plates means that they can be mounted on standard goniometers at most MX beamlines. The existing software for goniometer control can easily be adapted to automate crystal location and serial data collection. X-ray synchrotrons are generally accessible, in contrast to SFX beam time at FEL sources, which is oversubscribed and not widely available.

4.1.5. Surrounding mesophase characterization. The IMISX method lends itself to recording information on the identity and microstructure of the mesophase that surrounds the crystal directly where it grew. The bathing mesophase acts as a reservoir from which proteins diffuse to the growing face of the crystal. Phase mensuration, by means of SAXS/WAXS, provides quantitative information regarding the influence of the precipitant and other environmental factors on phase behaviour, which can in turn be used for a more rational approach to crystallogenesis.

4.1.6. COC sandwich plates. COC film, at 25 µm thick as used in the current IMISX application, is optically transparent, non-birefringent and has very low UV absorbance. In

several regards, therefore, it is similar to glass. Optical transparency is a particular advantage because, combined with the optical clarity of the cubic mesophase itself, it means that crystals of single-digit micrometre dimensions can be observed using a light microscope with relative ease. This facilitates screening for crystal growth in an imager. More importantly, it allows rapid and definitive crystal 'picking' with the on-axis microscope at the beamline for subsequent SX measurements. This obviates the need to perform diffraction raster scanning to locate crystals, which generates vast numbers of images that must be evaluated and can damage the crystals and the mesophase.

The windows of the IMISX plates are flat and scattering from the mesophase bolus is not masked in any way. As a result, crystal diffraction data can be collected at extremely wide angles without compromising the resolution. Because the windows are flat and optically transparent, refraction, which plagues *in situ* data collection in traditional plastic plates, is not an issue. By contrast, Axford *et al.* (2012) reported that in certain cases less than 20% of the images recorded contributed to the final merged *in situ* data set because of refraction in curved crystallization wells.

The fact that the IMISX inner plates have thin plastic windows means that they are readily opened with a scalpel, a blade or scissors for ligand or heavy-atom soaking and for harvesting for standard snap-cooling and data collection at 100 K where necessary.

4.1.7. Sealed double-sandwich plates. As a result of being doubly sealed, the plates are safe in that they effectively contain any toxic, hazardous or infectious materials that might be present in the mesophase or precipitant solution. This makes them much simpler and safer to handle, to ship and to work with at beamlines, where 'health and safety' are legitimate concerns. The outer glass plates are extremely robust, which makes the IMISX plates easily handled and shipped.

4.1.8. Viscous, sticky mesophase. The cubic phase is noted for being viscous and sticky. Accordingly, movement of the bolus in the well, which could potentially damage or cause loss of the crystals during shipping and handling, is not a problem. This translates to diffraction data collection, where the plates must be oriented vertically. Because the mesophase is viscous and sticky it resists movement under gravity, as do the crystals suspended in the mesophase. Therefore, mounting and rotating the plate during data collection can be performed in the knowledge that the crystal will remain in place. Such is not necessarily the case with *in situ* measurements made with crystals grown in a liquid. The sponge phase, which is a more fluid variant of the cubic mesophase, is less forgiving but is still useful for IMISX measurements, as demonstrated in the current study with AlgE and $PepT_{St}$.

4.1.9. Measurement at room temperature. Cooling crystals to 100 K for data collection can introduce strain and perturb packing, leading to a large mosaic spread and a possible reduction in diffraction quality and resolution. By making measurements directly at RT, as implemented here, the intrinsic quality of the crystal is maintained. This generally translates to considerably lower mosaic spread, as observed in the current study. Low mosaic spread is important when working with crystals with large unit cells, where overlaps can present problems, as in virus and ribosome crystallography. In addition, low mosaicity translates to more fully recorded reflections in partial data sets of narrow angular coverage. This in turn improves the quality of the processed data.

4.1.10. Conditions and results translate. For the membrane proteins examined in this study, the conditions that generated crystals by the standard *in meso* method translate to those under which IMISX trials were conducted. This means that the environment provided by the wells in COC plates contained within the sealed glass-sandwich plate is similar to that in the wells of standard glass-sandwich plates. Further, the crystal-growth characteristics, size and frequency appear to match between the two plate types. These results mean that moving from one approach to the other should be straightforward, without the need for extensive rescreening and optimization.

4.1.11. Data completeness, multiplicity and quality. In conventional crystallography, where diffraction data are collected from a single crystal by the rotation method, data completeness and multiplicity are determined by the point-group symmetry of the crystal, the angular coverage and the starting angle of the rotation (Dauter & Dauter, 1999). Data quality, as assessed by the internal consistency of symmetry-related reflections and the agreement between averaged measurements of the same reflection, is expressed by various R factors and a correlation coefficient (Diederichs & Karplus, 1997; Karplus & Diederichs, 2012).

In SX, a merged diffraction data set is obtained by combining many partial data sets (stills in SFX) collected from randomly orientated crystals. For merged data sets obtained with randomly oriented crystals, the multiplicities in SX follow a binomial distribution,

$$B(n, p, k) = \binom{n}{k} p^k (1-p)^{n-k}. \quad (1)$$

n is the number of asymmetric units in reciprocal space sampled by the data sets. This is the number of single data sets times twice the number of noncentring symmetry operators; the factor of two accounts for the two-dimensional X-ray detector, which is positioned symmetrically with respect to the origin of the diffraction pattern. p is the fraction of 180° covered by the effective oscillation range of a single data set. Since partials at the beginning and end of each data set do not contribute, the effective rotation range is less than the actual rotation range of the measurement. The value of p, and hence the effective rotation range, may be estimated by the average multiplicity of the merged data equalling $n \times p$. k is the multiplicity.

The fraction of unique reflections missing from the merged data set is estimated by $B(n, p, 0)$. As an example, in the lowest symmetry space group, $P1$, where 180° of data are needed for a complete data set, 1° of $P1$ data covers $p = 1/180 = 0.5555\%$ of the asymmetric unit in reciprocal space. Therefore, a single 1° data set collected using a symmetrically positioned detector would miss $(1 - 1/180)^2 = 98.89\%$ of the reflections of a hemisphere. In space group $P4_32_12$, 180° of data corresponds

to eight asymmetric units of reciprocal space since there are eight symmetry operators. Therefore, in the case of lysozyme, 1° of data fails to cover $B(8 \times 2, 1/180, 0) = (1 - 1/180)^{8 \times 2} = 91.47\%$ of all data. In the 113 native lysozyme data sets of 1.2° data each, we expect not to cover $(1 - 1.2/180)^{(8 \times 2 \times 113)} = 0.0006\%$ of all data. This corresponds to a completeness of 99.9994%; the observed value was 99.7%. However, this calculation is an overestimate because it neglects the fact that a 1.2° data set does not include partials on either side of a scan. From the observed average multiplicity of the merged data, we estimate that the effective rotation range for a 1.2° data set is 0.86°.

The observed multiplicities of acentric reflections in SX data collected from Lyso-Native, Lyso-Br, Lyso-S, $PepT_{St}$ and AlgE are plotted together with the corresponding binomial distributions (Fig. 5). For comparison, the multiplicity of a complete lysozyme data set collected from a single crystal is also shown. As predicted by binomial statistics, the distribution of multiplicity is broader and the average multiplicity is lower in SX data when compared with conventional crystallographic data (Fig. 5*a*). The binomial distribution agrees well with the observed multiplicity for Lyso-Native, Lyso-Br, Lyso-S and $PepT_{St}$ (Figs. 5*a*–5*d*). For AlgE, the observed multiplicity has a broader distribution owing to a preferred crystal orientation, which results in lower completeness (zero multiplicity) and more reflections with lower multiplicity, while the maximum multiplicity is higher (Fig. 5*e*).

In the last two decades, data-collection strategies have generally been biased towards obtaining high-dose data sets with minimum multiplicity from a single crystal. This approach, which is used primarily to minimize R_{sym}, often leads to unnecessary radiation damage. Recently, a paradigm shift has taken place. Thus, low-dose together with high-multiplicity data from multiple orientations of a single crystal and/or from multiple randomly oriented crystals have improved data accuracy by averaging out both random and systematic measurement errors (Diederichs, 2010; Liu *et al.*,

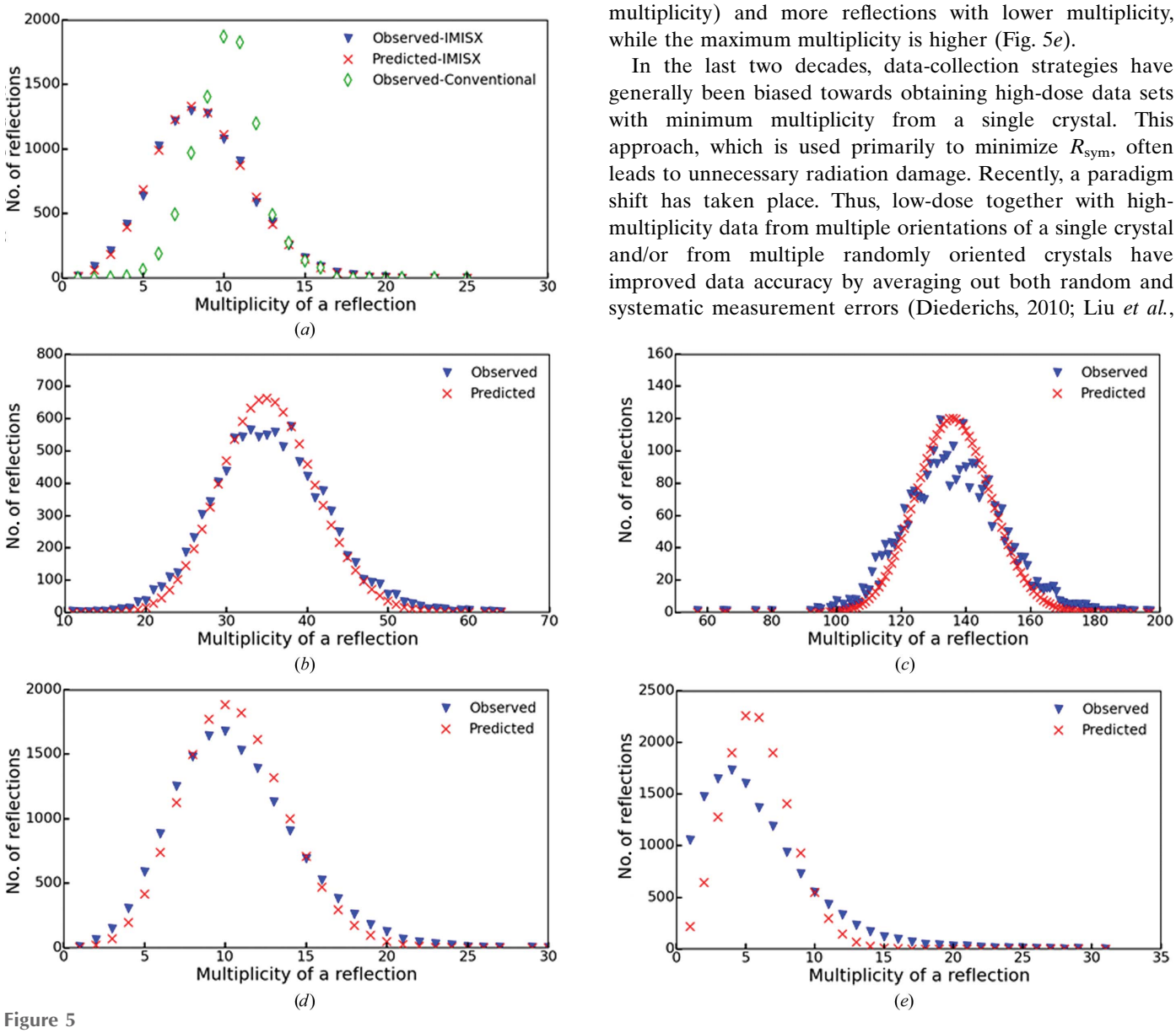

Figure 5
Observed and predicted distributions of reflection multiplicity in IMISX data sets recorded from lysozyme, $PepT_{St}$ and AlgE crystals at room temperature. Blue, multiplicity observed for IMISX data set. Red, binomial distribution of multiplicity predicted for a defined effective crystal rotation range. Green, multiplicity observed for a native lysozyme data set collected by conventional crystallography with a single crystal. (*a*) Lysozyme native SX data sets recorded with 113 crystals and an effective rotation range of 0.86°. (*b*) Lysozyme bromine SAD SX data sets recorded with 239 crystals and an effective rotation range of 1.66°. (*c*) Lysozyme sulfur SAD SX data sets recorded with 992 crystals and an effective rotation range of 1.55°. (*d*) $PepT_{St}$ native SX data sets recorded with 572 crystals and an effective rotation range of 0.42°. (*e*) AlgE native SX data sets recorded with 175 crystals and an effective rotation range of 0.76°.

2012; Weinert *et al.*, 2015). The success of sulfur SAD phasing with our 992-crystal SX data set has demonstrated that diffraction intensities could be extracted with very high accuracy from partial data sets of hundreds of micro-crystals. In contrast to the old model with its R_{sym}-centric focus on the precision of unmerged data (observations), the new insight highlights indicators that assess the precision and accuracy of merged data as being of particular utility in evaluating data quality. After all, it is these that are used for the downstream steps in structure solution and refinement. Indeed, statistical selection and merging of many 'weak' data sets improves the overall data quality. For example, although R_{meas}, which quantifies the agreement of the unmerged data, is around 10% in the low- to medium-resolution shells for the 992-crystal SX sulfur SAD data set (10% is considered to be high for conventional crystallography data), $R_{p.i.m.}$, which measures the precision of the merged data, is about 1.4%. This means that the measurement is more precise than the estimated intensity difference of 2.8% for a Bijvoet ratio of 1.4% from the anomalous signals of sulfur and chloride in lysozyme.

Although considered to be radiation damage-free, XFEL diffraction measurements (SFX) are limited to stills that amount to partial reflections. By contrast, IMISX allows the controlled recording of a number of sequential frames of between fractions of a degree to several degrees before radiation damage sets in. Coupled with integration and merging, this enables full reflection intensity reckoning, which is important for scaling and requires less data.

4.2. Challenges

At RT, where the current IMISX measurements were made, radiation damage severely limits the amount of data forthcoming from a given crystal. As a result, only small angular wedges of data could be collected from a given crystal and many wedges had to be recorded, indexed and aggregated from multiple, randomly oriented crystals for a full structure-factor set. In this work, wedges ranged from 0.6 to 2.0°, with the number of crystals required for a full data set ranging from 113 for lysozyme and 572 for PepT for MR phasing to 992 for lysozyme sulfur SAD phasing. Radiation damage sets in gradually in the course of data collection and there is no clear boundary between useful and useless frames. Although radiation damage cannot be avoided with synchrotron radiation, the next generation of fast X-ray detectors operating at kilohertz frame rates, such as EIGER (Johnson *et al.*, 2012), will enable the progression of radiation damage for each crystal to be monitored (§3.6, Supplementary Fig. S9). This quantitatively measured diffraction decay could in turn be exploited in subsequent data treatment (Ravelli *et al.*, 2003).

The current IMISX method was designed for use with crystals that grow at 20°C and for data collection at 20°C. However, not all crystals grow optimally at this temperature. As often as not, we find that the best crystals grow at 4°C. Regardless of what temperature is optimal, if this is different from the beamline-hutch temperature (∼20°C) then making measurements at the hutch temperature will impact on the mesophase microstructure and possibly its stability, both of which are temperature-sensitive. With 9.9 MAG as the host lipid, for example, raising the temperature anywhere in the range from 4 to 90°C will cause the mesophase to shed water (aqueous phase; Qiu & Caffrey, 2000) and for droplets to appear in the bolus. This makes it more difficult to locate crystals for data collection and may damage the crystals. It is therefore apparent that for optimal use of crystals grown by the *in meso* method, IMISX data collection at crystal-growth temperatures must be provided for.

Shipping harvested crystals to a synchrotron in Dewars at liquid-nitrogen temperature is routine and reliable. This is not the case for samples that must be shipped at closer to ambient temperatures, as is the case with the current IMISX plates. The special packing and packaging required to ensure delivery at controlled, but nonstandard, temperatures can complicate and increase the cost of shipping. Solutions to these challenges are in development.

Crystals that are harvested and placed in a Dewar under liquid nitrogen can be stored safely until beamtime becomes available. Such long-term storage is not generally an option when working with samples for *in situ* measurement, which have finite life times that can range from days to months at the growth temperatures. It is obvious therefore that having reliable and frequent access to a suitable X-ray source for data collection, on an as-needed basis, will contribute to the success of the *in situ* approach.

Data collection with single, pin-mounted crystals using a synchrotron micro-beam is routine. This is not the case for the crystals in plates for use in *in situ* measurements. Special plate grippers and high-precision and high-accuracy goniometers are needed along with appropriate on-axis, high-magnification microscopes and software to facilitate serial data collection from pre-selected crystals. Support for such measurements at synchrotron facilities worldwide is likely to be forthcoming in light of the data reported here and elsewhere demonstrating the power and utility of the *in situ* approach.

4.3. Quo vadis?

What we report here amounts to a demonstration study. Because of its success, IMISX is being used in projects in the MS&FB laboratory on a regular basis. We are now working to implement an IMISX application that is simple, robust, routine and, importantly, high throughput. To be accepted by the community at large, in addition to demonstrating that the method works reliably, as in this study, ideally it should be made easy to use and inexpensive. This may require improvements in plate design, as outlined below. It will certainly benefit from support for *in situ* work at synchrotron facilities through the provision of appropriate beamline plate hotels/imagers/incubators, robots, goniometers, on-axis microscopes and software.

Currently, ligand-binding screening assays performed *in meso* require the merging of data collected from as many as 50–100 crystals to obtain a structure with recognizable ligand density. Each one of these crystals must be harvested indivi-

dually from plates, snap-cooled and diffraction-rastered to locate and to centre the crystal for data collection. Given the inefficiency of the harvesting process, this translates to several hundreds of wells that have to be opened and from which crystals, tediously, have to be harvested. The process may need to be repeated at different ligand concentrations, with the result that many hundreds of wells with crystals may need to be processed to obtain a useful result. This in turn could translate into the need to set up certainly tens and possibly hundreds of plates. Using the IMISX method, it should be possible to directly collect the requisite data from the crystal manifest of just one to several wells without the need for harvesting.

Valuable beam time can be saved by performing the crystal selection or picking step off-line. Fiducials will be needed, ideally on each well, with which to align the sample in the beam for subsequent serial diffraction data collection. With automated data gathering, the method lends itself to an entirely automated process with little or no human intervention for the most efficient use of valuable beam time and other resources. Automation could usefully be extended to the evaluation of diffraction data in, or close to, real time to ensure that sufficient, but not too much, data of the right quality has been collected for the task at hand. Ideally, such measurements should be possible *via* remote access.

An alternative to hand-picking crystals is to use fast, fixed or helical line-scanning, as implemented recently for SX measurements at synchrotron (Gati *et al.*, 2014) and FEL sources (Hunter *et al.*, 2014). While this is likely to speed up diffraction data collection and reduce beam-time requirements, the burden shifts to needing efficient data acquisition, storage, processing and analysis, the latter two ideally in live time.

As noted, the *in meso* method works with soluble proteins. In the current study, lysozyme was used as a model soluble protein, and for the purposes of IMISX testing crystals were grown *in meso*. It is also possible to use the LCP as an inert, viscous medium in which to suspend extant crystals of soluble proteins for delivery or presentation to an interrogating X-ray beam. This approach and variations on it (Sugahara *et al.*, 2015) have been used to advantage for SX at FEL and synchrotron X-ray sources. The same method can be implemented for IMISX, where the attractive features of SX data collection, which works with micrometre-sized crystals, are exploited.

In situ data collection should be possible not just at RT but over a range of temperatures from RT down to 4°C and indeed to cryogenic temperatures. This is important for targets where crystals grow best at 4 or 10°C, for example. If it were possible to flash-cool individual IMISX wells in liquid nitrogen and to collect data at 100 K, the lifetime of the crystal would be extended by 30 to 50 times compared with RT, with the attendant reduction in the number of crystals required to complete a data set. Developments to realise these objectives are in progress.

While the focus has been on synchrotron sources, it is expected that the IMISX plates introduced here will prove to be useful with conventional X-ray sources. The latest models come with impressive brightness, flux and reduced beam sizes. At a minimum, therefore, *in situ* screening for crystal hits should be possible, with showers of microcyrstals giving rise to powder patterns. In the best of cases, structures may well be accessible. The real benefit, of course, comes from being able to make the measurements at home.

With weakly scattering crystals and for demanding crystallographic measurements, such as native SAD phasing, signal to noise must be optimized. For IMISX, as implemented here, this can be performed with thinner samples and window materials which lessen beam attenuation and scattering. With crystals that typically range from 10 to 30 µm in the maximum dimension, the mesophase thickness could likely be reduced from 64 µm, the minimum implemented in this study, by a factor of two without compromise. However, any reductions to where the thickness approaches the crystal size would have to be performed with due recognition that it could lead to preferential crystal orientation, with negative consequences for data completeness. Thinning the COC sheet further from its current thickness of 25 µm is an option, but will mean that the windows are that much more porous. As alternatives, graphene and silicon nitride windows, both of which are intrinsically watertight and can be made extremely thin, are being investigated.

The membrane-protein crystals used in this study ranged from 10 to 30 µm in the maximum dimension. While these are small, being able to work with even smaller crystals, of the type that often emerge as initial hits, would be advantageous. For such an application, thinner boluses and thinner windows for improved signal to noise would be desirable. The provision of a smaller, higher flux beam would also be important. These advances, coupled with a faster detector, would support measurements of unprecedented quality and enable measurements in the crystal size domain of 2 µm where photoelectron escape is possible (Sanishvili *et al.*, 2011) and in the time interval before the consequences of radiation damage become detrimental. Such developments are in progress.

5. Related literature

The following references are cited in the Supporting Information for this article: Caffrey (1987), Caffrey *et al.* (2009) and Coleman *et al.* (2004).

Acknowledgements

The authors thank A. Brinth, O. Abramczyk, S. Newstead and S. Shah for initial support in protein purification and production, provision of plasmids and lipid synthesis, N. Howe for help with plate design and testing, L. Vogeley for help with lysozyme–bromine sample preparation, Dectris Ltd for providing the EIGER 1M detector, C. Schulze-Briese and M. Mueller (Dectris) and A. Casanas (PSI) for help with data collection using the EIGER detector and M. Marsh and L. Vera for help with UV fluorescence microscopy and the SLS crystallization facility. This work was funded in part by grants from Science Foundation Ireland (12/IA/1255) and the National Institutes of Health (GM75915, P50GM073210 and

U54GM094599). PM was supported by a grant (WELBIO CR-2012S-04) to C. Govaerts (Université Libre de Bruxelles) from the Belgian National Funds for Scientific Research. X-ray diffraction data were collected on the PX II beamline at the Swiss Light Source, Villigen, Switzerland.

References

Adams, P. D., Grosse-Kunstleve, R. W., Hung, L.-W., Ioerger, T. R., McCoy, A. J., Moriarty, N. W., Read, R. J., Sacchettini, J. C., Sauter, N. K. & Terwilliger, T. C. (2002). *Acta Cryst.* D**58**, 1948–1954.

Aherne, M., Lyons, J. A. & Caffrey, M. (2012). *J. Appl. Cryst.* **45**, 1330–1333.

Axford, D. *et al.* (2012). *Acta Cryst.* D**68**, 592–600.

Barends, T. R. M., Foucar, L., Botha, S., Doak, R. B., Shoeman, R. L., Nass, K., Koglin, J. E., Williams, G. J., Boutet, S., Messerschmidt, M. & Schlichting, I. (2014). *Nature (London)*, **505**, 244–247.

Bingel-Erlenmeyer, R., Olieric, V., Grimshaw, J. P. A., Gabadinho, J., Wang, X., Ebner, S., Isenegger, A., Schneider, R., Schneider, J., Glettig, W., Pradervand, C., Panepucci, E. H., Tomizaki, T., Wang, M. & Schulze-Briese, C. (2011). *Cryst. Growth Des.* **11**, 916–923.

Botha, S., Nass, K., Barends, T. R. M., Kabsch, W., Latz, B., Dworkowski, F., Foucar, L., Panepucci, E., Wang, M., Shoeman, R. L., Schlichting, I. & Doak, R. B. (2015). *Acta Cryst.* D**71**, 387–397.

Boutet, S. *et al.* (2012). *Science*, **337**, 362–364.

Bricogne, G. (1993). *Acta Cryst.* D**49**, 37–60.

Caffrey, M. (1987). *Biochemistry*, **26**, 6349–6363.

Caffrey, M. (2015). *Acta Cryst.* F**71**, 3–18.

Caffrey, M. & Cherezov, V. (2009). *Nature Protoc.* **4**, 706–731.

Caffrey, M., Li, D., Howe, N. & Shah, S. T. A. (2014). *Philos. Trans. R. Soc. Lond. B Biol. Sci.* **369**, 20130621.

Caffrey, M., Lyons, J., Smyth, T. & Hart, D. J. (2009). *Curr. Top. Membr.* **63**, 83–108.

Chapman, H. N. *et al.* (2011). *Nature (London)*, **470**, 73–77.

Cheng, A., Hummel, B., Qiu, H. & Caffrey, M. (1998). *Chem. Phys. Lipids*, **95**, 11–21.

Cherezov, V. & Caffrey, M. (2003). *J. Appl. Cryst.* **36**, 1372–1377.

Cherezov, V. & Caffrey, M. (2007). *Faraday Discuss.* **136**, 195–212.

Cherezov, V., Peddi, A., Muthusubramaniam, L., Zheng, Y. F. & Caffrey, M. (2004). *Acta Cryst.* D**60**, 1795–1807.

Cipriani, F., Röwer, M., Landret, C., Zander, U., Felisaz, F. & Márquez, J. A. (2012). *Acta Cryst.* D**68**, 1393–1399.

Cohen, A. E. *et al.* (2014). *Proc. Natl Acad. Sci. USA*, **111**, 17122–17127.

Coleman, B. E., Cwynar, V., Hart, D. J., Havas, F., Mohan, J. M., Patterson, S., Ridenour, S., Schmidt, M., Smith, E. & Wells, A. J. (2004). *Synlett*, **8**, 1339–1342.

Dauter, Z. & Dauter, M. (1999). *J. Mol. Biol.* **289**, 93–101.

Diederichs, K. (2010). *Acta Cryst.* D**66**, 733–740.

Diederichs, K. & Karplus, P. A. (1997). *Nature Struct. Mol. Biol.* **4**, 269–275.

Dinapoli, R., Bergamaschi, A., Henrich, B., Horisberger, R., Johnson, I., Mozzanica, A., Schmid, E., Schmitt, B., Schreiber, A., Shi, X. & Theidel, G. (2011). *Nucl. Instrum. Methods Phys. Res. A*, **650**, 79–83.

Emsley, P. & Cowtan, K. (2004). *Acta Cryst.* D**60**, 2126–2132.

Fenalti, G. *et al.* (2015). *Nature Struct. Mol. Biol.* **22**, 265–268.

Fowler, P. W., Orwick-Rydmark, M., Radestock, S., Solcan, N., Dijkman, P. M., Lyons, J. A., Kwok, J., Caffrey, M., Watts, A., Forrest, L. R. & Newstead, S. (2015). *Structure*, **23**, 290–301.

Fraser, J. S., van den Bedem, H., Samelson, A. J., Lang, P. T., Holton, J. M., Echols, N. & Alber, T. (2011). *Proc. Natl Acad. Sci. USA*, **108**, 16247–16252.

Gati, C., Bourenkov, G., Klinge, M., Rehders, D., Stellato, F., Oberthür, D., Yefanov, O., Sommer, B. P., Mogk, S., Duszenko, M., Betzel, C., Schneider, T. R., Chapman, H. N. & Redecke, L. (2014). *IUCrJ*, **1**, 87–94.

Henke, B. L., Gullikson, E. M. & Davis, J. C. (1993). *At. Data Nucl. Data Tables*, **54**, 181–342.

Heymann, M., Opthalage, A., Wierman, J. L., Akella, S., Szebenyi, D. M. E., Gruner, S. M. & Fraden, S. (2014). *IUCrJ*, **1**, 349–360.

Holton, J. M. (2009). *J. Synchrotron Rad.* **16**, 133–142.

Hunter, M. S. *et al.* (2014). *Sci. Rep.* **4**, 6026.

Johnson, I., Bergamaschi, A., Buitenhuis, J., Dinapoli, R., Greiffenberg, D., Henrich, B., Ikonen, T., Meier, G., Menzel, A., Mozzanica, A., Radicci, V., Satapathy, D. K., Schmitt, B. & Shi, X. (2012). *J. Synchrotron Rad.* **19**, 1001–1005.

Karplus, P. A. & Diederichs, K. (2012). *Science*, **336**, 1030–1033.

Keedy, D. A., van den Bedem, H., Sivak, D. A., Petsko, G. A., Ringe, D., Wilson, M. A. & Fraser, J. S. (2014). *Structure*, **22**, 899–910.

Kmetko, J., Warkentin, M., Englich, U. & Thorne, R. E. (2011). *Acta Cryst.* D**67**, 881–893.

Leal, R. M. F., Bourenkov, G., Russi, S. & Popov, A. N. (2013). *J. Synchrotron Rad.* **20**, 14–22.

Li, D., Boland, C., Aragao, D., Walsh, K. & Caffrey, M. (2012). *J. Vis. Exp.*, e4001.

Li, D., Boland, C., Walsh, K. & Caffrey, M. (2012). *J. Vis. Exp.*, e4000.

Liu, Q., Dahmane, T., Zhang, Z., Assur, Z., Brasch, J., Shapiro, L., Mancia, F. & Hendrickson, W. A. (2012). *Science*, **336**, 1033–1037.

Liu, W. *et al.* (2013). *Science*, **342**, 1521–1524.

Lyons, J. A., Parker, J. L., Solcan, N., Brinth, A., Li, D., Shah, S. T. A., Caffrey, M. & Newstead, S. (2014). *EMBO Rep.* **15**, 886–893.

Maeki, M., Yoshizuka, S., Yamaguchi, H., Kawamoto, M., Yamashita, K., Nakamura, H., Miyazaki, M. & Maeda, H. (2012). *Anal. Sci.* **28**, 65.

McCoy, A. J., Grosse-Kunstleve, R. W., Adams, P. D., Winn, M. D., Storoni, L. C. & Read, R. J. (2007). *J. Appl. Cryst.* **40**, 658–674.

Nogly, P. *et al.* (2015). *IUCrJ*, **2**, 168–176.

Owen, R. L., Axford, D., Nettleship, J. E., Owens, R. J., Robinson, J. I., Morgan, A. W., Doré, A. S., Lebon, G., Tate, C. G., Fry, E. E., Ren, J., Stuart, D. I. & Evans, G. (2012). *Acta Cryst.* D**68**, 810–818.

Perry, S. L., Guha, S., Pawate, A. S., Henning, R., Kosheleva, I., Srajer, V., Kenis, P. J. A. & Ren, Z. (2014). *J. Appl. Cryst.* **47**, 1975–1982.

Pineda-Molina, E., Daddaoua, A., Krell, T., Ramos, J. L., García-Ruiz, J. M. & Gavira, J. A. (2012). *Acta Cryst.* F**68**, 1307–1310.

Pinker, F., Brun, M., Morin, P., Deman, A.-L., Chateaux, J.-F., Oliéric, V., Stirnimann, C., Lorber, B., Terrier, N., Ferrigno, R. & Sauter, C. (2013). *Cryst. Growth Des.* **13**, 3333–3340.

Qiu, H. & Caffrey, M. (2000). *Biomaterials*, **21**, 223–234.

Ravelli, R. B. G., Leiros, H.-K. S., Pan, B., Caffrey, M. & McSweeney, S. (2003). *Structure*, **11**, 217–224.

Roversi, P., Blanc, E., Vonrhein, C., Evans, G. & Bricogne, G. (2000). *Acta Cryst.* D**56**, 1316–1323.

Sanishvili, R., Yoder, D. W., Pothineni, S. B., Rosenbaum, G., Xu, S., Vogt, S., Stepanov, S., Makarov, O. A., Corcoran, S., Benn, R., Nagarajan, V., Smith, J. L. & Fischetti, R. F. (2011). *Proc. Natl Acad. Sci. USA*, **108**, 6127–6132.

Sheldrick, G. M. (2010). *Acta Cryst.* D**66**, 479–485.

Stellato, F. *et al.* (2014). *IUCrJ*, **1**, 204–212.

Sugahara, M. *et al.* (2015). *Nature Methods*, **12**, 61–63.

Tan, J., Rouse, S. L., Li, D., Pye, V. E., Vogeley, L., Brinth, A. R., El Arnaout, T., Whitney, J. C., Howell, P. L., Sansom, M. S. P. & Caffrey, M. (2014). *Acta Cryst.* D**70**, 2054–2068.

Tilton, R. F. Jr, Dewan, J. C. & Petsko, G. A. (1992). *Biochemistry*, **31**, 2469–2481.

Warkentin, M., Hopkins, J. B., Badeau, R., Mulichak, A. M., Keefe, L. J. & Thorne, R. E. (2013). *J. Synchrotron Rad.* **20**, 7–13.

Weierstall, U. *et al.* (2014). *Nature. Commun.* **5**, 3309.

Weinert, T. *et al.* (2015). *Nature Methods*, **12**, 131–133.

Woldeyes, R. A., Sivak, D. A. & Fraser, J. S. (2014). *Curr. Opin. Struct. Biol.* **28**, 56–62.

Yin, X., Scalia, A., Leroy, L., Cuttitta, C. M., Polizzo, G. M., Ericson, D. L., Roessler, C. G., Campos, O., Ma, M. Y., Agarwal, R., Jackimowicz, R., Allaire, M., Orville, A. M., Sweet, R. M. & Soares, A. S. (2014). *Acta Cryst.* D**70**, 1177–1189.

BIOLOGICAL
CRYSTALLOGRAPHY

Volume 71 (2015)

Supporting information for article:

In meso in situ serial X-ray crystallography of soluble and membrane proteins

Chia-Ying Huang, Vincent Olieric, Pikyee Ma, Ezequiel Panepucci, Kay Diederichs, Meitian Wang and Martin Caffrey

S1. Materials

Monoolein (9.9 MAG) (M239-F4-X) was purchased from Nu-Chek Prep (Elysian, MN) and 7.8 MAG (smm48 and C84) was synthesized and purified in-house, following established procedures (Coleman *et al.*, 2004; Caffrey *et al.*, 2009). Chicken egg white lysozyme (Cat. L6876, lot SLBG8654V), HEPES (Cat. H4034, lot SLBF8768V), sodium acetate (Cat. S2889, lot 079K0122), PEG 400 (Cat. 81172, lot BCBL5307V), sodium bromide (Cat. 71329, lot 132896), hydrochloric acid (Cat. 07102, lot SZBL2500V), ammonium phosphate dibasic (Cat. 09839, lot BCBK1426V) and ammonium phosphate monobasic (Cat. 216003, lot MKBJ9529V) were obtained from Sigma (St. Louis, MO). Sodium chloride (BP358-212, lot 132896) was from Fisher Scientific (Loughborough, U.K.). Microsyringes (Cat. 81030) were sourced from Hamilton (Bonaduz, GR, Switzerland). Cyclic olefin copolymer (COC, Cat. TOPAS 8007) and harvesting cryo-loops (Cat. M2-L18SP-20, M2-L18SP-30 and M2-L18SP-50) were purchased from MiTeGen (Ithaca, NY). Standard glass (127.8 × 85.5 mm^2, 1 mm thick; Cat. 1527127092, lot 29642819) and No. 1.5 glass (124 × 84 mm^2, 0.15 mm thick; Cat. 01029990933, lot 30129819) were obtained from Marienfeld (Lauda-Königshofen, Germany). Perforated double-stick spacer tape (112 × 77 mm^2) of varying thicknesses (50, 64, 140 μm and perforation diameters (6 and 7 mm) (Cat. 9500PC and 9009), and double-stick gasket (2 mm-wide and 140 μm-thick with outer dimensions 118 × 83 mm^2 and inner dimensions 114 × 79 mm^2; TRI-9500PC) were purchased from Saunders (St. Paul, MN). Glass cutters (TCT Scriber & Glass Cutter, Cat. 633657) were obtained from Silverline (Yeovil, UK). Rain-X rain repellent (Cat. 80199200, lot 5026349013414) was from Shell Car Care (*Altrincham*, *Cheshire*, U.K.).

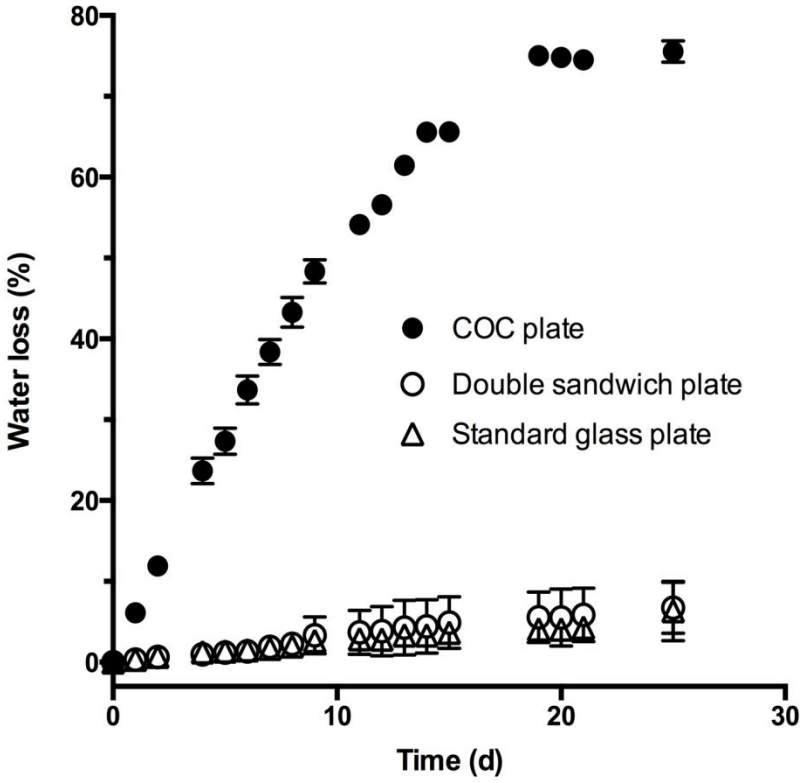

Figure S1 Time-dependent loss of water from COC sandwich plates, double sandwich IMISX plates and standard glass sandwich plates at 20 °C. Measurements were made with 96-well plates stored in a temperature-regulated incubator with 800 nL precipitant solution in each well as described under Methods. The total mass of precipitant on a plate as a function of time was recorded over a period of 25 days. Precipitant mass at time zero was approximately 70 mg.

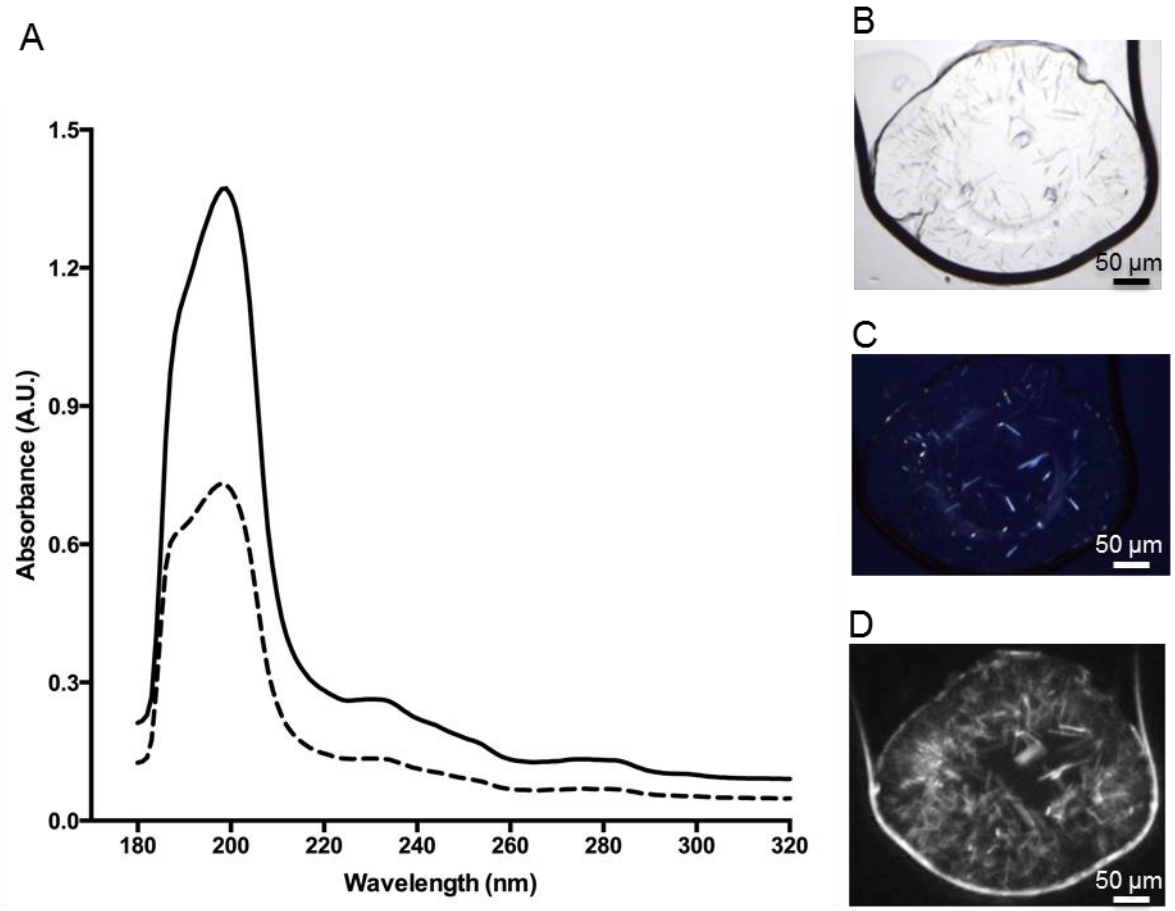

Figure S2 Spectral absorbance, transmission and transparency properties of COC film and plates used for IMISX measurements. (*A*) Absorption spectrum of one (dashed line) and two pieces (solid line) of COC film, 25 µm-thick, as used in IMISX plates. Spectra were recorded against air. Images of membrane protein crystals growing in the cubic phase housed in COC sandwich plates recorded by bright field (*B*) and cross polarized light microscopy (*C*) and by UV fluorescence microscopy (*D*). Images were recorded using a Rockimager 1000 (Formulatrix) that included an ultraviolet imaging device.

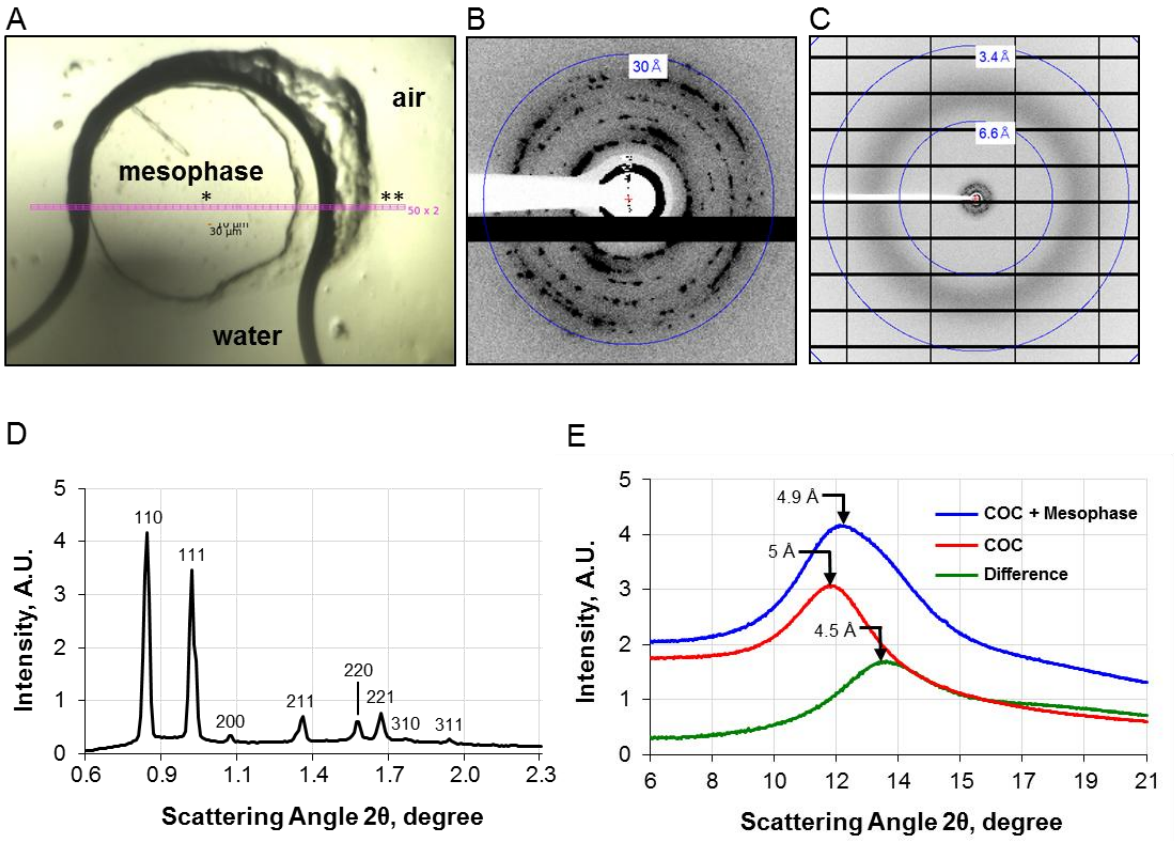

Figure S3 SAXS and WAXS from the cubic-Pn3m phase of fully hydrated 9.9 MAG in an IMISX well at room temperature. (*A*) IMISX sample used for SAXS/WAXS reference measurements mounted on a goniometer at beamline PXII (X10SA) viewed through the COC window with an on-axis microscope. The horizontal two-row grid identifies the section of the sample used for SAXS measurements made with a 30 × 10 μm^2 beam in sequential horizontal steps of 30 μm and an exposure time of 0.1 s at a sample-to-detector distance of 490 mm and a wavelength of 1.0331 Å. The sample was prepared by incubating a 200 nL bolus of molten 9.9 MAG in 1 μL Milli-Q water sealed in an IMISX well for 3 hours at room temperature. Sample thickness was 190 μm which included the 50 μm of COC film and 140 μm of mesophase. (*B*) SAXS pattern recorded in the grid sector marked with an asterisk in (*A*). The resolution marker (circular dashed line) corresponds to 30 Å. The spotty SAXS pattern derives from microdomains of which the liquid crystalline sample is constituted. (*C*) WAXS and SAXS pattern recorded as in (*B*) with resolution markers at 6.6 and 3.4 Å. (*D*) Circular averaging of the SAXS pattern in (*B*) with data presented in the form of an intensity versus *d*-spacing and scattering angle (I/2θ) plot. Low-angle powder peaks, identified by Miller indices (*hkl*), index in the cubic-*P*n3m space group with *d*-spacing values of 71.2 Å (*110*), 58.63 Å (*111*), 50.93 Å (*200*), 41.05 Å (*211*), 35.79 Å (*220*), 33.88 Å (*221*), 32.16 Å (*310*) and 29.45 Å (*311*) and relative *d*-spacing values of 1.00, 1.21, 1.40, 1.73, 1.99, 2.10, 2.21 and 2.42, respectively. For a cubic space group, the unit cell parameter, *a*, equals $d(h^2 + k^2 + l^2)^{1/2}$. A line of best fit to data plotted as *d* versus ($h^2 + k^2 +$

$l^2)^{-1/2}$ for the 8 peaks has a slope a = 101.3 Å (r^2 = 0.9997). A similar value has been reported for fully hydrated 9.9 MAG in sealed glass X-ray capillaries at 20 °C (Caffrey, 1987). The black ring to the center of the pattern is due to X-ray scattering from and leakage around the beamstop. (*E*) Circular averaging of the WAXS region of the pattern in (*C*) with data presented as in (*D*). Patterns were recorded in the sample at grid sectors marked by single and double asterisks in (*A*) corresponding to mesophase plus COC windows (blue line) and to COC windows alone (red line), respectively. A difference I/2θ profile corresponding to scattering from the mesophase alone is included (green line). COC has a diffuse scattering peak centered at ~5.0 Å. Scattering from 'molten' chains in the mesophase is also broad, with a maximum at ~4.5 Å, as observed previously (Caffrey, 1987).

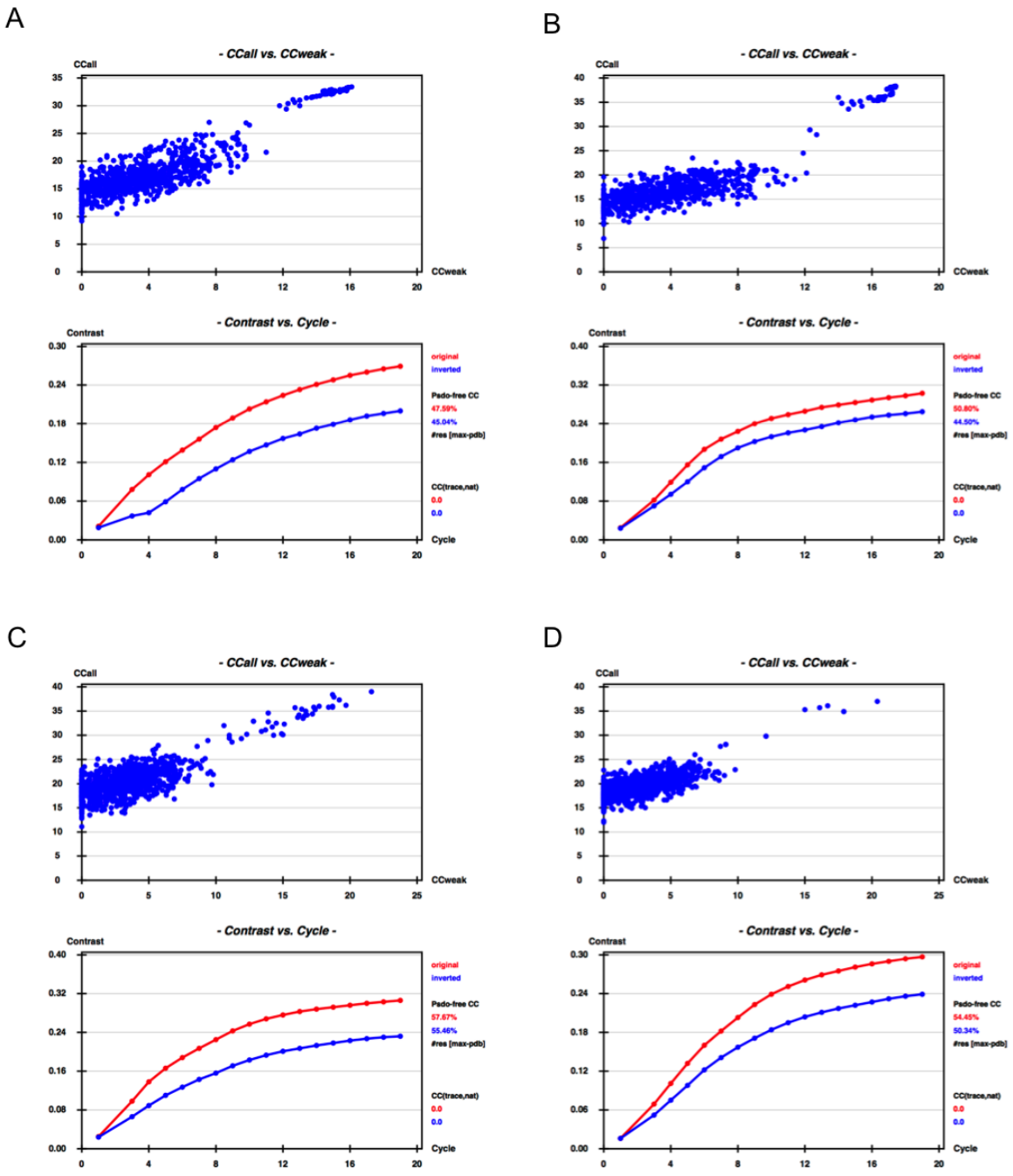

Figure S4 Substructure and hand determination with SHELXD/E. (*A*) Lysozyme Br-SAD IMISX data. (*B*) Lysozyme Br-SAD 100 K data. (*C*) Lysozyme S-SAD IMISX data. (*D*) Lysozyme S-SAD 100 K data.

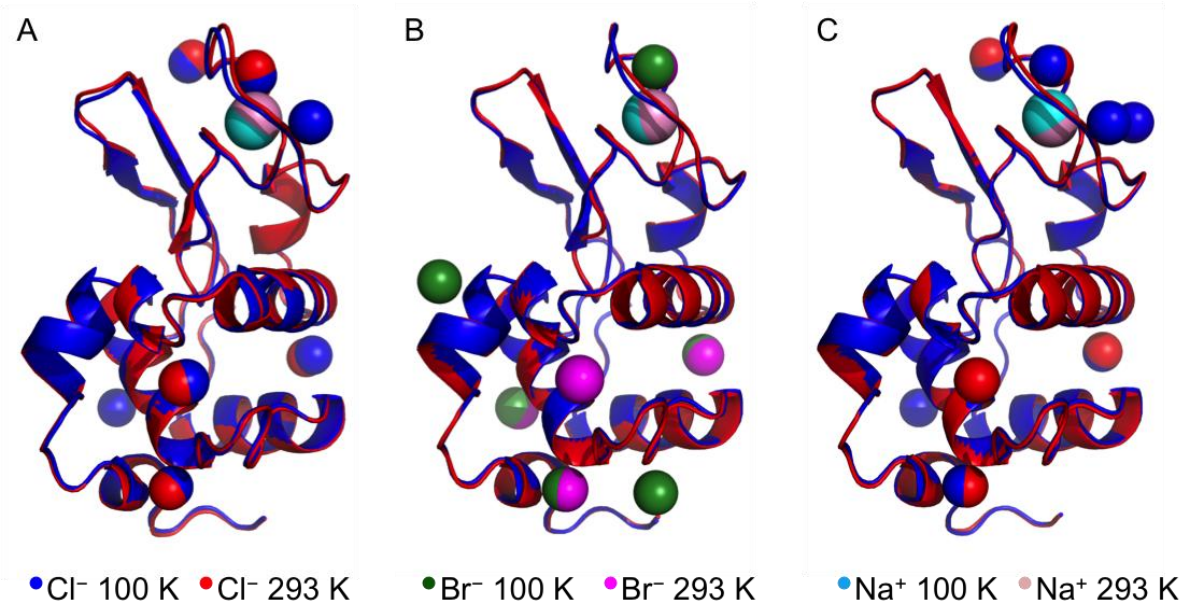

Figure S5 Structure of lysozyme solved by molecular replacement (*A*), Br-SAD (*B*) and S-SAD phasing (*C*) using *in situ* crystals at room temperature (red ribbon model) and harvested crystals at 100 K (blue ribbon model). Structured ions are shown as spheres coloured as follows: chloride, blue (100 K) and red (293 K); bromide, green (100 K) and magenta (293 K); sodium, light blue (100 K) and pink (293 K). The r.m.s.d. over 129 residues for backbone atom positions between 100 K and 293 K models obtained by molecular replacement, Br-SAD and S-SAD phasing were 0.257 Å, 0.169 Å and 0.196 Å, respectively.

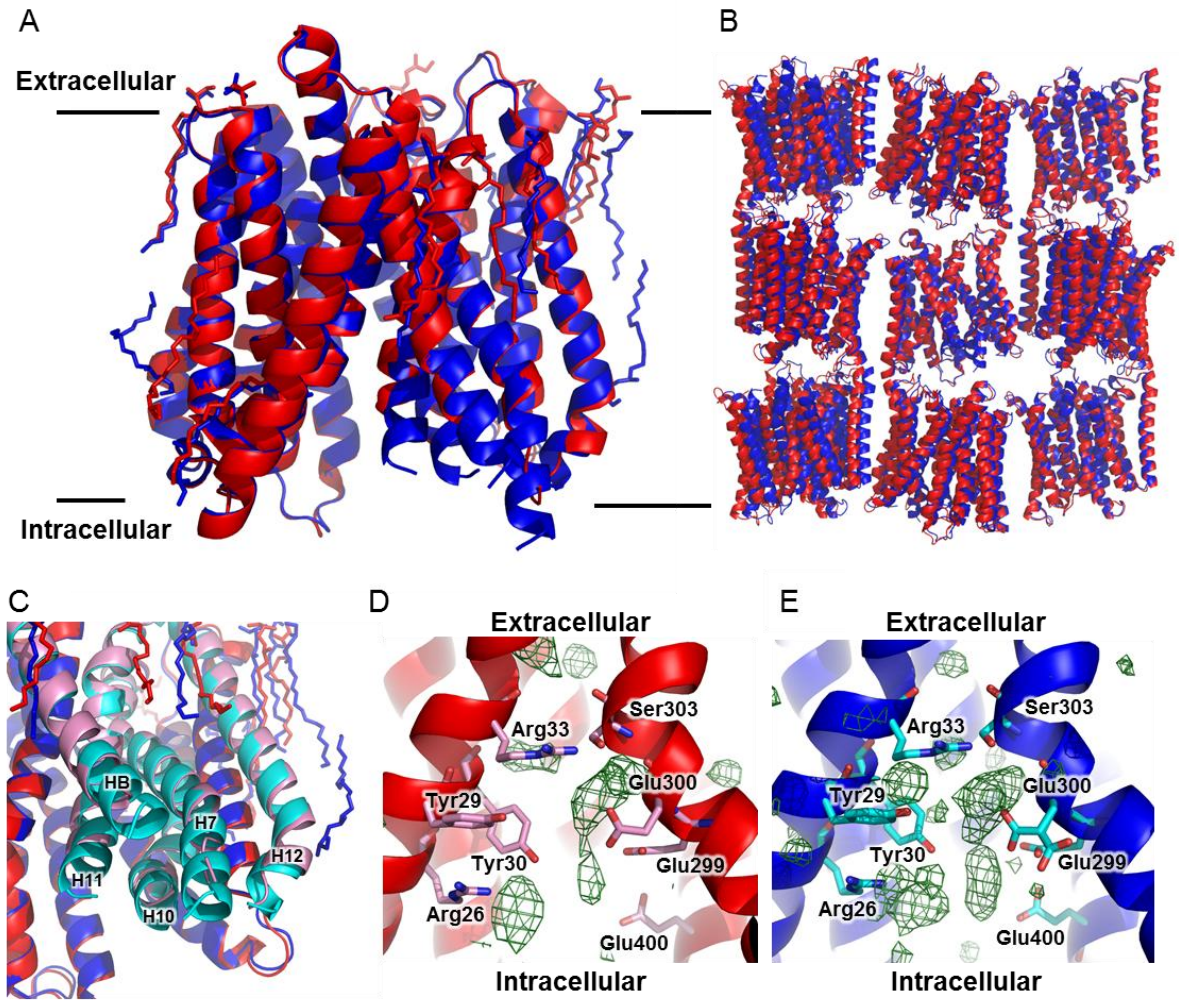

Figure S6 A comparison of the structures of $PepT_{St}$ obtained using IMISX at room temperature and by conventional cryo-crystallography at 100 K. (*A*) Superposition of $PepT_{St}$ structures at room temperature (red) and at 100 K (blue). The view is from within the membrane, the approximate limits of which are marked by horizontal black lines. Lipid and detergent molecules are in stick representation. (*B*) The packing arrangement in crystals of $PepT_{St}$. Room temperature and 100 K structures are shown superposed with color coding as in (*A*). The layered or Type I packing is typical of *in meso* grown crystals. (*C*) An expanded view of parts of the $PepT_{St}$ that differ in structure between that recorded at room temperature and at 100 K. Sections of the protein that show differences are colored pink and light blue corresponding to structures at room temperature and 100 K, respectively. Helix (H) identities are as described in the text. A view into the 'peptide' binding pocket of $PepT_{St}$ at room temperature (*D*) and at 100 K (*E*) revealing unaccounted for electron density (green mesh; Fo−Fc omit density maps contoured at 3 σ) referred to in the text. Conserved residues proposed to partake in peptide binding and transport are identified and shown in stick representation.

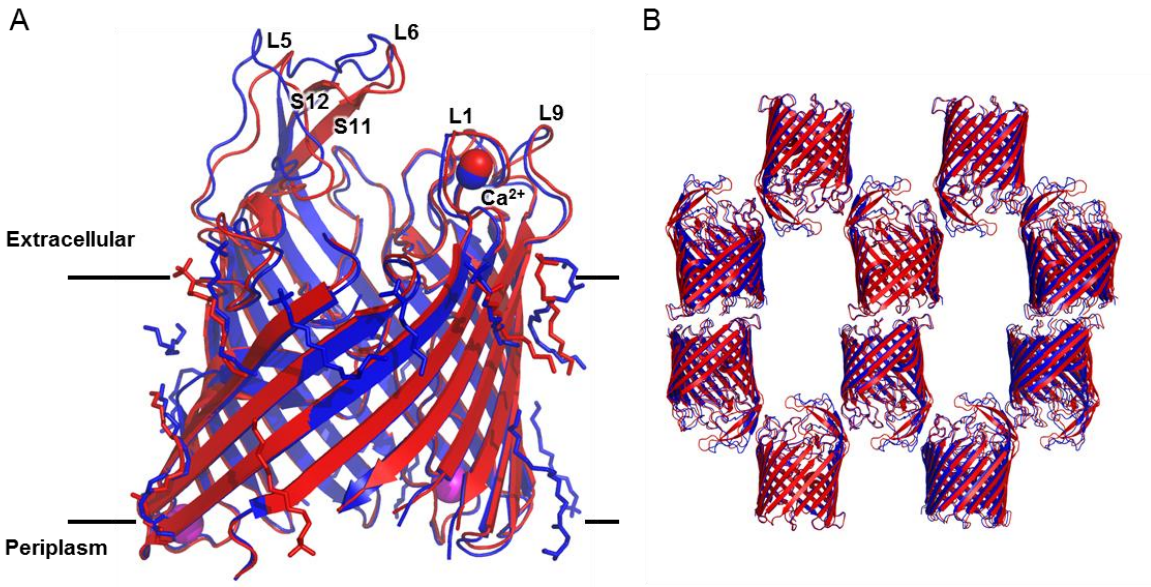

Figure S7 A comparison of the structures of AlgE obtained using IMISX at room temperature and by conventional cryo-crystallography at 100 K. (*A*) Superposition of AlgE structures at room temperature (red) and at 100 K (blue). The view is from within the membrane, the approximate limits of which are marked by horizontal black lines. Lipid and detergent molecules are shown as stick figures and calcium as spheres. Copper has been reported to occupy the calcium site in L1. An X-ray fluorescence scan performed on an AlgE crystal in an IMISX well at room temperature showed no evidence for copper. The density was best explained by calcium. Extracellular loops (L1, L5, L6, L9) and β-strand (S11 and S12) that differ between the two data set types and/or that are involved in crystal contacts are labelled. The two sodium cations were colored magenta which only showed in room temperature structure. (*B*) The packing arrangement in crystals of AlgE. Room temperature and 100 K structures are shown superposed with color coding as in (*A*). Crystal contacts on the extracellular side of AlgE involve loops L5 and L6 and β-strand S11 and S12 of one molecule and L1 and L9 of another.

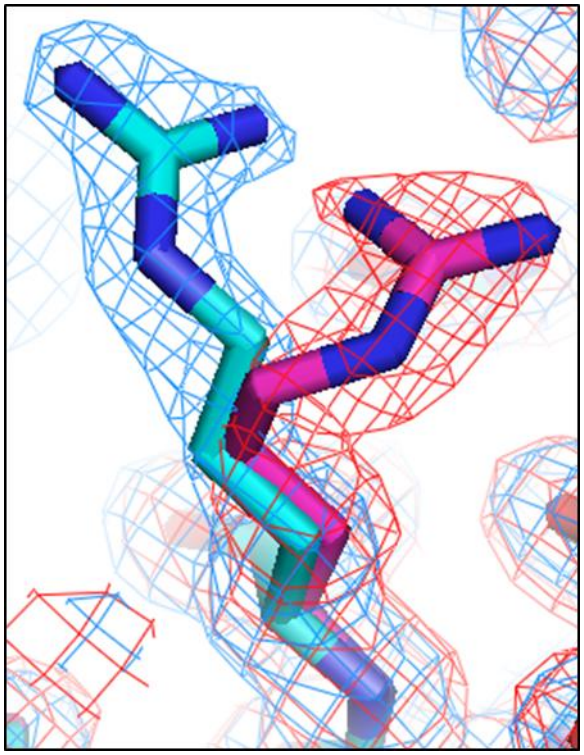

Figure S8 Alternative conformations observed for the side chain of Arg112 in native lysozyme crystals at room temperature (magenta) and at 100 K (light blue). Electron density maps are shown as red and light blue meshes contoured at 1 σ. Stick representation is shown (carbon, red and light blue; nitrogen, blue). Arg112 is located on the surface of lysozyme to the periphery of the substrate binding cleft.

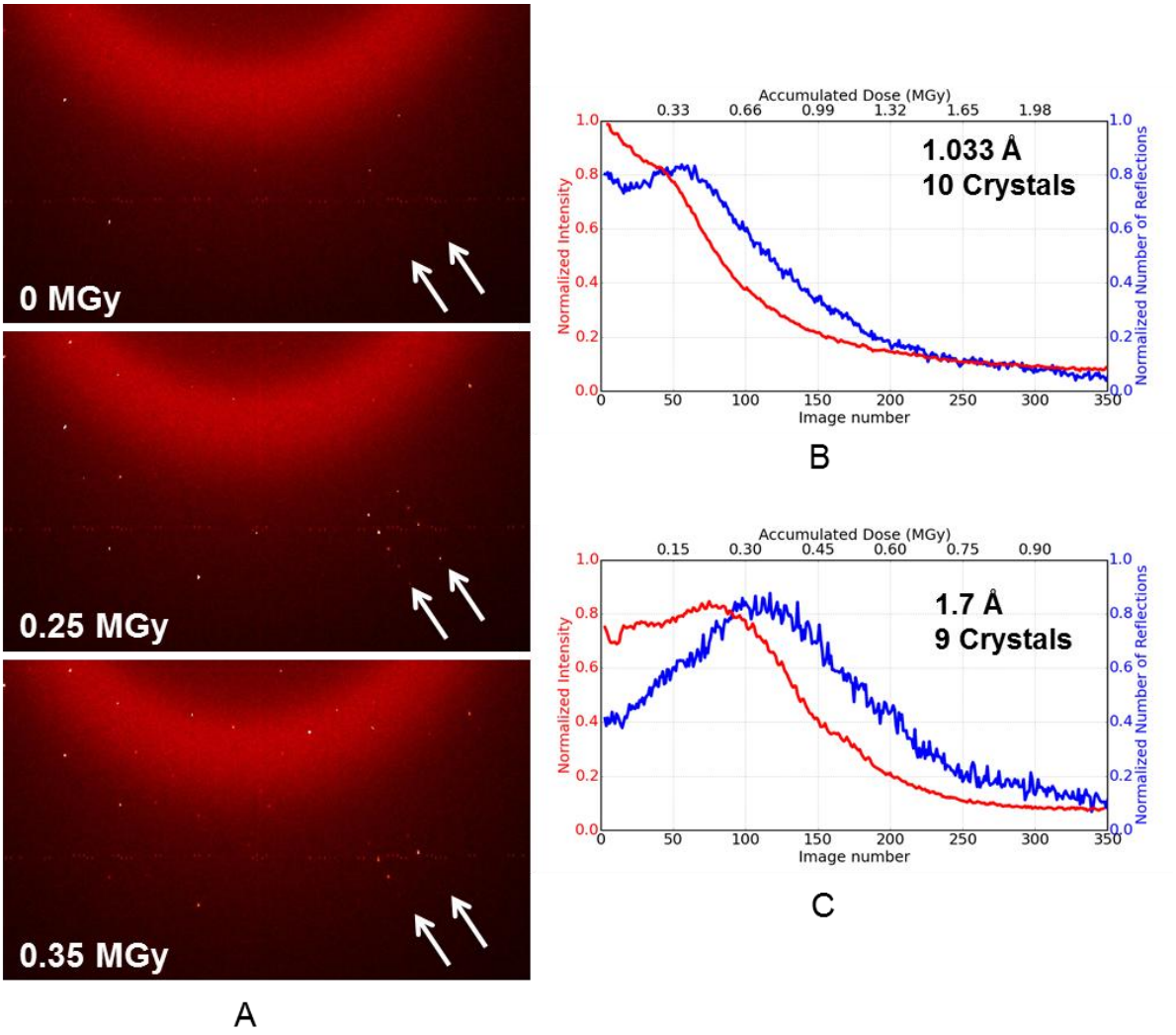

Figure S9 The effect of accumulated X-ray dose on diffraction characteristics of native lysozyme crystals in IMISX plates at room temperature. Crystals were stationary and were not rotated during the course of the exposure. (*A*) Diffraction at wide angles recorded from a single, fixed crystal at increasing accumulated dose at 1.7 Å. Images shown are the sum of five sequential frames. The arrows point in directions where the coming and going of reflections due to radiation damage is particularly apparent. Diffuse scatter from the COC windows and the mesophase reaches a maximum at around 4.9 Å. (*B*, *C*) Normalized and averaged total crystal diffraction intensity and normalized number of reflections per image as a function of image number and accumulated dose. The total number and intensity of all reflections on each still image was calculated using custom spot finding and integration Python scripts. Total intensities were summed, normalized and averaged over all crystals (10 crystals at 1.033 Å, 9 crystals at 1.7 Å). There is a peak in number of reflections early in the exposure. This transient rise is attributed mainly to reciprocal lattice points that move into the Ewald sphere and into diffraction condition by the damage-induced increase in mosaicity. A 357-frame movie of diffraction images of the type represented in Fig. S9C? is included under Supplementary Movie.

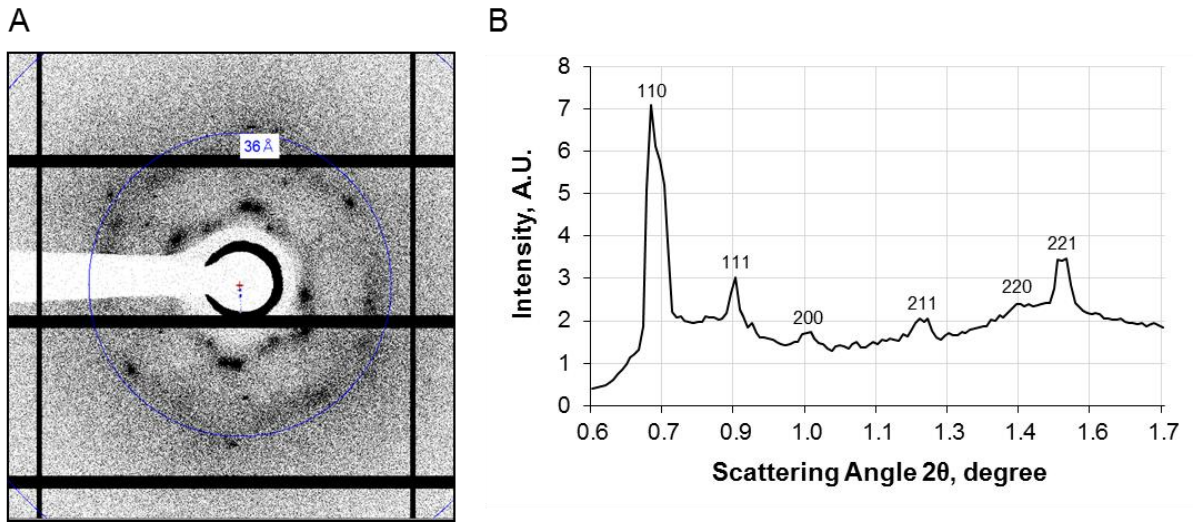

Figure S10SAXS from the cubic-Pn3m phase of fully hydrated 7.8 MAG in an IMISX well at room temperature. (*A*) SAXS pattern recorded as described in **Supplementary Fig. S3**. The resolution marker (blue circle) corresponds to 36 Å. (*B*) Circular averaging of the SAXS pattern in (*a*) with data presented as an I/2θ plot, as in **Supplementary Fig. S3**. Low-angle powder peaks, identified by Miller indices, index in the cubic-*P*n3m space group with *d*-spacing values of 83.06 Å (*110*), 67.09 Å (*111*), 58.15 Å (*200*), 47.47 Å (*211*), 40.57 Å (*220*) and 38.34 Å (*221*) and relative *d*-spacing values of 1.00, 1.24, 1.43, 1.75, 2.05 and 2.17, respectively. The corresponding unit cell parameter, *a*, calculated as in the legend to **Supplementary Fig. S3**, is 115.5 Å (r^2 = 0.9992). The black ring to the center of the pattern is due to X-ray scattering from and leakage around the beamstop.

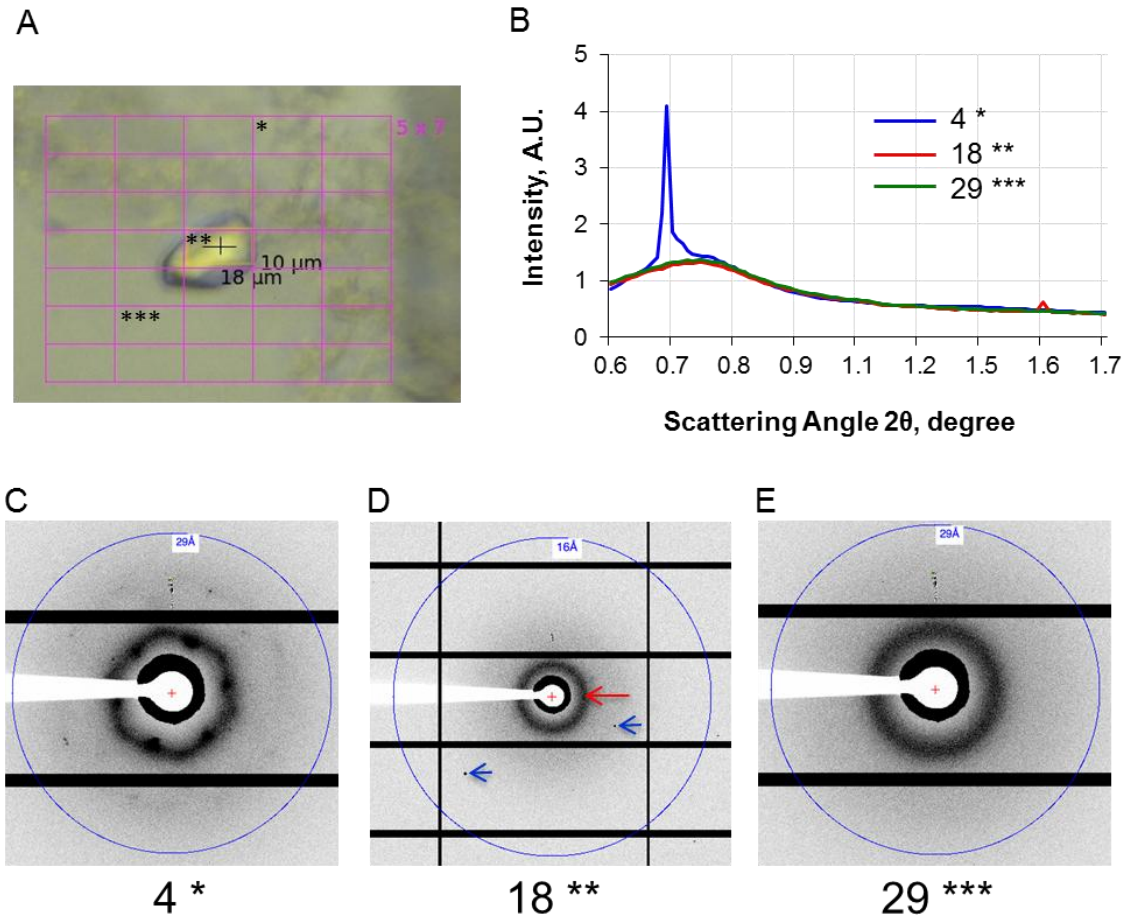

Figure S11 SAXS characterization of the mesophase in the vicinity of a $PepT_{St}$ crystal in an IMISX well at room temperature with 7.8 MAG as the host lipid. The precipitant included 250–325 mM $NH_4H_2PO_4$, 100 mM HEPES, pH 7.0 and 21–22 %(*v*/*v*) PEG 400. (*A*) View of a crystal growing in the mesophase, with a rastering grid superimposed, in preparation for SAXS measurements. The beam and raster sector sizes are 18 × 10 µm^2. I/2θ plot (*B*) of the SAXS data recorded on sample in (*A*) at grid sectors 4 (blue line) (*C*), 18 (red line) (*D*) and 29 (green line) (*E*), as in **Supplementary Fig. S3**. The diffuse low-angle band, with a scattering maximum at ~75 Å, derives from the sponge phase (red arrow in (*D*). The sharp reflections derive from the $PepT_{St}$ crystals (blue arrows in *D*). The diffuse scatter and sharp peaks in the profile recorded in sector 4 indicate that the sponge and cubic phases coexist at this location in the sample. Assuming the latter is of the cubic-*Pn3m* type, it indexes with a unit cell length of 115.9 Å (see legend, **Supplementary Fig. S3**). At locations in the sample corresponding to sectors 18 and 29, the sponge phase alone is present.

Table S1 Facts and figures used to estimate the accumulated dose per crystal for the IMISX data recorded and the radiation damage study performed at 293 K

Experiment	IMISX					Radiation damage study	
Protein	Lyso-Native	Lyso-Br	Lyso-S	$PepT_{St}$**	AlgE	Lyso-Native	Lyso-S
Crystal size (μm^3)	10×10×20	10×20×30	10×10×20	10×10×20	5×5×20	20×20×40	20×20×40
Wavelength (Å)	1.0332	0.9205	1.7000	1.0332	1.0332	1.0332	1.7000
Energy (keV)	12.000	13.469	7.293	12.000	12.000	12.000	7.293
Flux (photons/s)	3×10^{11}	1.5×10^{10}	9×10^{9}	3×10^{11} 7.5×10^{10}	1.5×10^{11}	3×10^{12}	5×10^{11}
Beam size (μm^2)	10 × 18	10 × 18	10 × 30	10 × 18	10 × 10	10 × 50	10 × 50
Estimated dose rate (MGy/s)*	0.889	0.083	0.042	0.889 0.222	0.800	3.202	1.445
Oscillation / exposure (° / s)	0.2 / 0.05	0.1 / 0.1	0.1 / 0.1	0.2 / 0.05 0.1 / 0.1	0.2 / 0.05	0	0
Oscillation range/crystal (°)	1.2	2	2	0.6	1	0	0
Exposure time/ crystal (s)	0.3	2.0	2.0	0.15 0.6	0.25	1	1
Estimated accumulated dose/crystal (MGy)*	0.267	0.166	0.084	0.133 0.133	0.200	3.3	1.5
Total number of crystals	113	239	992	237 335	175	–	–
Total degree/ data set (°)	113	478	1984	142.2 201	175	–	–
Total exposure time/data set (s)	33.9	478	1,984	236.6	43.8	–	–
Total dose/data set (MGy)	30	39	83	76	35	–	–

* estimate based on Equation 1 in Holton (Holton, 2009). For Lyso-Br crystals at the Br K-edge, the 'dose-doubling' effect of an estimated 0.38 M bromide in the crystal, assuming a solvent content of 38%, has been accounted for. Solvent content was calculated based on a combined lysozyme + 51 structured waters molecular weight of 15,191 Da and the Matthews Probability Calculator (http://www.ruppweb.org/mattprob/default.html)

** two different flux and oscillation/exposure values used

Table S2 Sample consumption and diffraction measurement statistics

Supplementary Table S2

Temperature /Presentation	100 K / Loop					293 K / *In situ*				
Protein	Lyso-Native	Lyso-Br	Lyso-S	$PepT_{St}$	AlgE	Lyso-Native	Lyso-Br	Lyso-S	$PepT_{St}$	AlgE
MAG	9.9	9.9	9.9	7.8	7.8	9.9	9.9	9.9	7.8	7.8
Mesophase/well (nL)	200	200	200	66	50	200	200	200	66	50
Lipid/protein soln (by vol.)	3/2	3/2	3/2	1/1	1/1	3/2	3/2	3/2	1/1	1/1
Protein conc. (mg/mL)	50	50	50	10	10	50	50	50	10	10
No. wells	1	1	1	1	1	2	4	12	20	1
No. crystals	1	1	3	1	1	114	279	1,290	1,363	484
No. useful crystals	1	1	3	1	1	113	239	992	572	175
Index rate (%)	100	100	100	100	100	99.1	85.6	76.8	41.9	36.2
Lipid (μL)	0.12	0.12	0.12	0.033	0.025	0.24	0.48	1.44	0.66	0.025
Protein (μg)	4	4	4	0.33	0.25	8	16	48	6.6	0.25
Total degrees / crystal	100	720	360	120	140	2	2	2	1, 2*	3
Useful degrees / crystal	100	720	360	120	140	1.2	2	2	0.6	1
Oscillation (^{o} / frame)	0.1	0.1	0.1	0.1	0.5	0.2	0.1	0.1	0.1, 0.2*	0.2
Degrees (^{o}), total	100	720	1,080	120	140	135.6	478	1,984	343.2	175

***** Some crystals were measured with 0.1 ^{o} /frame, others were measured with 0.2 ^{o} /frame.

Table S3 Differences in lysozyme, $PepT_{St}$ and AlgE structures determined by the IMISX method at room temperature and by conventional crystallography in loops at 100 K.

(*a*) Lysozyme

Residue	**Differences, RT *vs*. 100 K**		
	Lyso-Native	**Lyso-Br**	**Lyso-S**
R14	*	**	*
L17	*	*	*
D18	***	**	**
N19	**	**	*
R21	*	*	*
R45	*	*	*
N46	*	-	-
T47	*	-	*
D48	*	-	-
I55	*	-	-
N59	*	**	-
R61	*	*	***
P70	*	-	-
R73	**	**	**
N77	***	***	**
S86	-	***	-
D87	**	*	-
D93	**	-	-
K97	*	**	****
D101	***	*	-
D103	*	*	*
V109	*	*	*
A110	*	-	-
R112	**	**	***
N113	*	*	-
D119	*	*	*
Q121	****	*	**
R125	*	*	**
R128	*	***	*
L129	*	**	*

- very similar to identical

* slightly different

** different conformers

*** multiple side chain conformers in the RT structure

**** poor electron density at this residue

(*b*) $PepT_{St}$.

Residue /Segment[a]	Features			Differences[d]
	RT[b]	**100 K[b]**	**100 K[c] PDB 4D2B**	
E300	Conf. A	Conf. A, B	Conf. A, B	***
N-ter.	G5-P12 (M1-K4)	G5-P12 (M1-K4)	K6-P12 (M1-G5)	*
H1	L13-T46	L13-T46	L13-T46	-
H2	R53-I81	R53-I82	T52-I81	-
H3	A84-A103	A84-A103	G83-L104	-
H4	A108-L136	A108-L136	G107-L136	*
H5	R142-A173	R143-A173	R143-A172	*
H6	Y175-T200	Y175-T200	G174-T200	-
HA	P214-V241	P214-V241	A213-V241	*
HB	L246-F265 (W267-H279)	L246-S270 (V272-V274)	S245-S270 (S271-H279)	**
H7	S284-E312	T277-E312	R281-V314	**
H8	V321-A345	V321-A345	P320-W343 (L346-A348)	*
H9	S353-Y378	S353-Y378	S352-G379	*
H10	P386-S409 (T411-M423)	P386-K413 (A415-F419)	P386-T412 (K413-Q422)	**
H11	S425-L444	S421-L444	M423-Y445	**
H12	S449-I475 (Q476-E483)	S449-G477 (M479-E483)	S449-L471 (K473-E483)	**

[a] notation as in Lyons *et al*., 2014

[b] this work. Missing residues are shown in closed brackets.

[c] this $PepT_{St}$-apo structure, from Lyons *et al*. (Lyons *et al*., 2014), is included as a reference. Missing residues are shown in closed brackets.

[d] comparing RT and 100 K structures reported in this work with the following structure difference ratings:

- little or no difference

* same secondary structure, but slightly misaligned

** residues missing and secondary structure changed

*** conformer differences. See Supplementary Fig. S6*D*, *E*.

(*c*) AlgE.

Residue /Segment[a]	**Features**			**Differences**[d]
	RT[b]	**100 K**[b]	**100 K**[c] **PDB 4AFK**	
N-ter.	P39-N41	P39-N41	E37-N41	-
S1	F42-E53	F42-N54	F42-N54	-
L1	N54-T65	D55-T65	D55-T65	***
S2	L66-Q80	L66-Q80	L66-W81	-
T1	W81--D83	W81--D83	G82-D83	-
S3	W84-A94	W84-A94	W84-A95	-
L2	A95-K123 (D107-P121)	A95-K123 (D109-P120)	T96-K123 (D109-N116)	**
S4	S124-D134	S124-D134	S124-Y135	-
T2	Y135- G143	Y135- G143	A136-G143	-
S5	E144- L153	E144-L153	E144-R154	-
L3	R154- Q161	R154-Q161	E160-Q161	-
S6	D162- P172	D162-P172	D162-E173	-
T3	E173-L176	E173-L176	T174-L176	*
S7	L177-A184	L177-A184	L177-Q185	-
L4	Q185-D203	Q185-D203	R186-D204	*
S8	R205-W215	R205-W215	R205-A216	-
T4	A216-H218	A216-H218	P217-H218	-
S9	H219-D229	H219-D229	H219-D230	*
L5	D230-G250	D230-G250	S231-T247	***
S10	Q251-T260	Q251-T260	Y248-G261	-
T5	G261-P271	G261-P271	D262-P271	-
S11	L272-T291	L272-N287	L272-T292	***
L6	V292-R297	L288-G301	V293-R296	***
S12	I298-W318	K302-W318	R297-N319	***
T6	N319-Q323	N319-Q323	I320-Q323	-
S13	W324-R332	W324-R332	W324-G333	-
L7	G333-S375	G333-N376	S334-N376	*
S14	N376-Q387	L377-Q387	L377-L388	-
T7	L388-E390	L388-E390	R389-D391	*
S15	D391-W402	D391-W402	Y392-R403	-
L8	R403-D425	R403-D425	V404-K424	*
S16	I426-K435	I426-K435	D425-Y437	-
T8	Y437-L457 (Q440-P454)	Y437-L457 (K439-P454)	F438-A456 (K439-P454)	**
S17	I458-K466	I458-K466	L457-P467	-
L9	P467-T478	P467-T478	G468-T478	***
S18	M479-W488	M479- R489	M479-R489	-
C-ter.	R489- F490	F490	F490	**

[d] comparing RT and 100 K structures reported in this work with the following structure difference ratings and notes:

- identical

* same secondary structure, but slightly misaligned align

** residues missing and secondary structure changed

*** involved in crystal contact

References

Caffrey, M. (1987). *Biochemistry* **26**, 6349-6363.

Caffrey, M., Lyons, J., Smyth, T. & Hart, D. J. (2009). *Curr. Top. Membr.* **63**. *83–108.*

Coleman, B. E., Cwynar, V., Hart, D. J., Havas, F., Mohan, J. M., Patterson, S., Ridenour, S., Schmidt, M., Smith, E. & Wells, A. J. (2004). *Synlett* **8**, 1339–1342.

Holton, J. M. (2009). *J. Synchrotron Radiat.* **16**, 133-142.

Lyons, J. A., Parker, J. L., Solcan, N., Brinth, A., Li, D., Shah, S. T., Caffrey, M. & Newstead, S. (2014). *EMBO rep.* **15**, 886-893.

Tan, J., Rouse, S. L., Li, D., Pye, V. E., Vogeley, L., Brinth, A. R., El Arnaout, T., Whitney, J. C., Howell, P. L., Sansom, M. S. & Caffrey, M. (2014). *Acta Cryst.* D**70**, 2054-2068.

Supplementary Movie

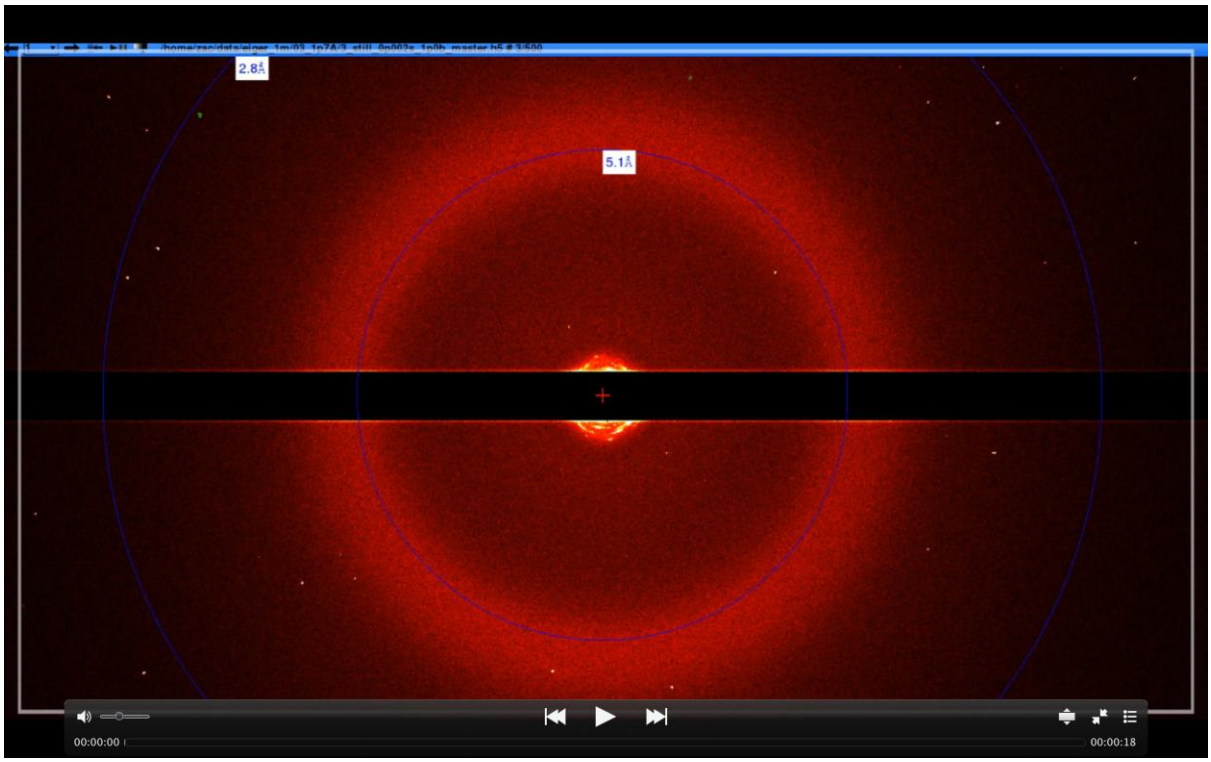

Still Image and Legend for Movie

Supplementary Movie S1. The effect of accumulated X-ray dose on diffraction characteristics of native lysozyme crystals in IMISX plates recorded at room temperature with the EIGER 1M detector operating at 500 images/second and a readout time of 20 μs. Crystals were stationary and were not rotated during the course of the exposure with a 10 × 50 μm^2 sized unattenuated beam at 1.7 Å. Diffuse scatter from the COC windows and the mesophase reaches a maximum at around 4.9 Å. See Fig. S9.